Progress in Oceanography 219 (2023) 103172

Contents lists available at ScienceDirect

Progress in Oceanography

journal homepage: www.elsevier.com/locate/pocean

Connecting subtropical salinity maxima to tropical salinity minima: Synchronization between ocean dynamics and the water cycle

Lisan Yu

Department of Physical Oceanography, Woods Hole Oceanographic Institution, Woods Hole, MA 02543, USA

ARTICLE INFO

Keywords:
Sea surface salinity
Tropical salinity minimum zones
Subtropical salinity maxima
Ekman transport
Satellite salinity missions
El Niño - Southern Oscillation

ABSTRACT

Recent satellite observations reveal that the annual cycles of tropical sea surface salinity (SSS) minimum (*Smin*) and subtropical SSS maximum (*Smax*) are phased locked, with the former leading the latter by six months. The evidence suggests an interconnected nature between the salinity extrema, motivating an investigation into the underlying mechanisms. It is found that the poleward Ekman transport, driven by trade winds, stands as a pivotal conduit linking the influence of tropical freshwater to high salinities in the subtropical oceans. Two key aspects are central to the operation of this advective oceanic pathway. One is the annual formation of the near-equatorial *Smin* zones by Ekman convergence of the freshwater sourced from the double Intertropical Convergence Zones. The other is the advection time taken by Ekman transport traveling at an average speed of approximately 7 cm s^{-1}. This speed allows the near-equatorial salinity anomalies to be carried to the subtropical *Smax* fringes in six months, aligning closely with the observed semi-annual phase shift between *Smin* and *Smax*. During El Niño - Southern Oscillation (ENSO) warm and cold episodes in recent decade, poleward propagation of near-equatorial low salinity anomalies was particularly prominent, leading to substantial surface freshening in the subtropical Pacific. Interestingly, the latitudinal spread of the ENSO-triggered SSS anomalies is confined within the domain of the poleward Ekman transport. This confinement reaffirms the inherent connection between the tropical *Smin* and subtropical *Smax* regions, shedding light on the intricate interplay between oceanic processes, the water cycle, and SSS distributions.

A Plain Language Summary

Traditionally, tropical salinity minima (*Smin*) and subtropical salinity maxima (*Smax*) are considered as separate entities due to their distinct characteristics and geographical separation. However, recent analysis of satellite sea surface salinity (SSS) observations reveals that the two SSS extrema are phase connected on an annual basis, with the tropical *Smin* leading the subtropical *Smax* by six months. Motivated by this compelling evidence, the present study sets to explore the interconnected nature of tropical and subtropical salinities and to identify the underlying mechanisms that govern this connection. The study found that the poleward Ekman transport, driven by the prevailing tropical trade winds, serves as an essential oceanic pathway, tying the influence of tropical freshwater to the subtropical oceans. The rainfall associated with the double Intertropical Convergence Zones provides the essential freshwater source for the formation of a *Smin* zone in each basin. Once formed, these near-equatorial salinity anomalies are transported poleward by Ekman currents, reaching the equatorial flanks of the subtropical *Smax* centers in about six months. The time required for Ekman salinity advection aligns closely with the observed six-month phase shift in the seasonal cycles between *Smin* and *Smax*. By elucidating this oceanic pathway, the study expands our understanding of the intrinsic connection between tropical low salinities and subtropical high salinities. These insights suggest the need to reevaluate methodologies for deriving information about changes in the ocean water cycle from SSS observations.

1. Introduction

One of the most striking features of global sea surface salinity (SSS) patterns is the contrast between the minimum SSS (hereafter *Smin*) in the tropical ocean and the maximum SSS (hereafter *Smax*) in the subtropical ocean. Excessive evaporation in subtropical high-pressure belts leads to salt build up at the surface, forming five subtropical *Smax* centers, one in each open basin (Gordon et al. 2015; Johnson et al. 2016). Conversely, excessive precipitation in the tropical ocean freshens surface waters, creating east–west aligned tropical *Smin* zones parallel to the Intertropical Convergence Zone (ITCZ) and South Pacific Convergence Zone (SPCZ) (Delcroix et al., 1996; Kao and Lagerloef, 2015; Yu

E-mail address: lyu@whoi.edu.

https://doi.org/10.1016/j.pocean.2023.103172
Received 27 May 2023; Received in revised form 24 October 2023; Accepted 9 November 2023
Available online 10 November 2023

2014; Martins and Stammer 2015; Guimbard et al. 2017). There exist also a regional *Smax* in the highly evaporative northern Arabian Sea (Rochford, 1964), and a *Smin* in the northern Bay of Bengal resulting from high riverine freshwater discharge (Rao and Sivakumar 2003). However, due to the influence of the seasonally reversing monsoon circulation (Schott and McCreary 2001; Phillips et al., 2021), the salinity extrema in the North Indian Ocean have seasonal characteristics different from those of open-ocean *Smax* and *Smin* (Yu et al. 2021) and hence, they are not included in the present study of the open-ocean salinity extrema.

Long-term change and variability of the *Smin* and *Smax* have been intensely studied, as salinity extrema and contrasts are not only useful proxy indicators of the global water cycle but also a major driver of the density-driven ocean circulation (Dickson et al. 1988; Schmitt, 2008; Durack et al., 2012). Over the last half-century, ocean salinity observations have revealed that salty subtropical regions have become saltier, while fresh tropical regions become fresher (Boyer et al. 2005; Durack and Wijffels 2010). This change pattern is regarded as oceanic evidence supporting the wet-gets-wetter and dry-gets-drier paradigm, showing that the water cycle's patterns of evaporation, water vapor transport through the atmosphere, and precipitation have been amplifying under the rising global temperatures (Held and Soden, 2006). However, despite salinity's potential as a proxy rain gauge (Zika et al., 2015; Cheng et al. 2020), questions still remain as to to what extent salinity "memorizes" the long-term water cycle changes (Terray et al. 2012; Vinogradova and Ponte, 2017; Yu et al. 2020).

Salinity variability is profoundly modulated by ocean advection and diffusion (mixing and vertical entrainment) (Kolodziejczyk and Gaillard 2013; Camara et al. 2015). One best example is the perpetual displacement of *Smax* on the poleward side of the net evaporation maxima. This location mismatch is attributed to the needed balance between the *E–P* flux and the rate at which SSS is redistributed by ocean advection and diffusion (Walin 1982; Schanze et al. 2010; Zika et al. 2015). Ponte and Vinogradova (2016) examined this balance in a global ocean state estimate produced by the consortium for Estimating the Circulation and Climate of the Ocean (ECCO) to understand the processes shaping mean SSS patterns. They found that although salinity anomalies induced by surface freshwater forcing can be mostly compensated by diffusion through mixing and vertical entrainment, ocean advection is quantitatively important for balancing the salinity budget. They showed that ocean advection is manifested by the westward and poleward displacement of peak SSS regions relative to the *E-P* maxima, consistent with various studies that identify Ekman salt transport as a primary vehicle for redistributing high-salinity surface waters away from their formation site near net evaporation maxima (e.g. Yu 2011; Bingham et al., 2012; Vinogradova and Ponte, 2013; Johnson et al. 2016; Melzer and Subrahmanyam 2017). Gordon et al. (2015) estimated the mean latitudinal position for all five open ocean *Smax* using the location of coinciding low SSS gradient bands. They showed that the *Smax* regime in the North Pacific and North Atlantic spreads between 20°N–30°N with a core at about 26°N. The *Smax* regime in the South Pacific and South Atlantic is about 5–6° of latitude closer to the equator, lying between 15°S–22°S around a core at 18°S. The *Smax* in the South Indian Ocean is the furthest from the equator among the five *Smax* regimes, falling between 26°S and 32°S around a center near 30°S. Several studies have speculated that differences in the latitudinal position of the five *Smax* centers may reflect the influence of ocean basin configuration on the interaction between surface waters and the regional water cycle (Nilsson et al. 2013; Jones and Cessi 2017). However, despite the position differences, the seasonal SSS cycle for all five *Smax* centers is surprisingly consistent, attaining a maximum in local fall and minimum in local spring (Gordon et al. 2015; Johnson et al. 2016). This complex set of characteristics suggest that the factors influencing *Smax* may include both internal dynamics and external forcing. Nonetheless, the internal governing processes have been less mentioned and studied.

The role of Ekman salt advection in poleward distribution of the tropical low salinity anomalies has garnered increasing attention recently. Using two-year satellite SSS observations from Aquarius/SAC-D, Yu (2014; 2015) showed that there is an annual formation of the salinity minimum zones of 50–80 m deep during August-September, induced by Ekman convergence of the freshwater sourced from the ITCZ. After formation, the salinity minimum zones do not remain near the ITCZ rain bands but are advected poleward by Ekman currents. Yu (2015) noted that the progression of the *Smin* zones is monotonically poleward, contrasting sharply to the seasonal north/south migration of the ITCZ. Several studies that analyzed observational datasets with longer records or used ocean model simulations have yielded a similar result, supporting the poleward propagation of the low-salinity anomalies of near-equatorial origin (e. g. Ren and Riser 2009; Bingham et al. 2012; 2019; Qu et al. 2011, 2013; Hasson et al. 2013; Tchilibou et al. 2015; Melnichenko et al. 2019; Aubone et al. 2021). Camara et al. (2015) examined the processes controlling the mixed layer salinity (MLS) seasonal budget in the tropical Atlantic Ocean using a regional ocean general circulation model (OGCM). They argued that the poleward transport of near-equatorial low-salinity waters is a way of the ocean to counterbalance the excessive high-salinity anomalies produced in the subtropical evaporative region. They also showed that the seasonal cycle of the dominant processes for the MLS budget, including the surface E-P flux, Ekman advection, vertical diffusion of salt at the base of the mixed layer, are all phased by the seasonal cycle of surface winds. The model-based results of Camara et al. are intriguing, as the phase locking of salinity generation, distribution, and dissipation to winds would imply that the trade winds are the ultimate driver of ocean adjustment to seasonal E-P forcing in the tropical-subtropical region.

The subtropical higher-salinity regime is receptive to salinity interannual variability of near-equatorial origin. Hasson et al. (2018) investigated the unexpected freshening event in 2014–2015 in the subtropical Pacific around the Hawaiian archipelago between 15°N and 25°N. They found that this persistent freshening was a superposition of SSS anomalies sourced from two El Niño events: the weak 2014 episode and the stronger 2015–2016 event. Both anomalies were advected northward in the tropical current system by the mean Ekman currents and, hypothetically, by instabilities in the zonal currents patterns, a process they termed the northward pathway for equatorial anomalies to reach the extratropics. Hasson et al. further analyzed the analogous structures in the past 20 years and suggested that the northward displacement of SSS anomalies is not specific to El Niño years, even though their advection is enhanced during El Niño events. These findings raise the question of whether the tropical salinity influence on the subtropical region is a result of internal dynamical feedback.

Recent annual harmonic analysis of satellite and Argo SSS observations (Yu et al. 2021) suggests that the tropical *Smin* and subtropical *Smax* may be intrinsically connected on an annual basis, as the analysis reveals a distinct six-month shift between the annual phases of the two SSS extrema in all five open basins. This study aims to explore the interconnected relationship between tropical and subtropical salinities. It will show that the primary mechanism governing this connection is the poleward Ekman advection of salinity anomalies originating near the equatorial latitudes. The presentation is organized as follows. Section 2 provides a brief description of data and methods used in the study. Section 3 presents the analysis of the connection pattern between *Smin* and *Smax*, the oceanic pathway enabled by the poleward Ekman transport, and the lagged phase synchronization in the annual cycles between *Smin* and *Smax*. Section 4 discusses the dynamical implications of the Ekman-enabled oceanic pathway. Summary and conclusion are included in section 5.

2. Data

2.1. Salinity datasets

Salinity observations has increased rapidly in recent decades, thanks to the advent of satellite salinity missions (Vinogradova et al. 2019; Reul et al. 2020) and the evolving capacities of the Argo profiling float network (Roemmich et al. 2019). Both satellite SSS and Argo subsurface salinity observations are used in the study. The SSS dataset is the satellite Multi-Mission Optimally Interpolated Sea Surface Salinity (OISSS) Global Dataset V1 (Melnichenko, 2021), which is a Level-4 product with a 0.25° spatial resolution and 4-day temporal resolution, covering the period from September 2011 to March 2022. The product is constructed from blending Level-2 swath data sourced from two satellite missions: the Aquarius/SAC-D (September 2011 - June 2015) and Soil Moisture Active Passive (SMAP; April 2015 to present). Measurements from ESA's SMOS mission (November 2009 to present) are used to fill in data gaps when the SMAP satellite was in safe mode without data delivery during June-July 2019. OISSS applies an optimally designed large-scale bias correction to reduce small-scale noises in SMAP SSS fields and enhance their spatial consistency with the Aquarius retrievals that have a coarser footprint resolution. The product is evaluated against in situ salinity from Argo floats and moored buoys, showing that the collocated OISSS and in situ measurements have a near-zero bias and a mean root-mean-square difference (RMSD) of 0.19 Practical Salinity Scale 1978 (hereafter pss).

Gridded Argo temperature and salinity products from Roemmich and Gilson (hereafter RG) (2009) are used for cross-validating the identified SSS patterns and providing the subsurface information needed in the analysis. The RG Argo products are constructed from more than 3,000 autonomous profiling floats over the global ocean. Time-mean field was first constructed using a weighted local regression fit to several years of Argo data and optimal interpolation was then applied to the mean-subtracted monthly residuals to obtain the interpolated anomaly fields on 1°×1° grids. The salinity data of the topmost layer at a depth of 2.5 m is regarded as SSS when comparing with satellite products.

2.2. Harmonic analysis

Harmonic analysis is a useful approach for identifying periodic patterns in time series data, particularly for capturing dominant characteristics of seasonal variability. This method has been used in various studies, such as Boyer and Levitus (2002), Rao and Sivakumar (2003), Bingham et al. (2012), Reagan et al. (2014), Köhler et al. (2015), Melnichenko et al. (2019), and Yu et al. (2021), to extract seasonal patterns from the salinity data. This method is applied here to aid the analysis of the SSS phase connection in the tropical-subtropical region.

At each grid location (x, y), the harmonic analysis decomposes the SSS time series into a series of sinusoidal functions, which can be expressed in the following form:

$$S(x,y,t) = \overline{S}(x,y) + \sum_k \left(A_k(x,y)\cos\left(\frac{2\pi kt}{T}\right) + \varphi_k(x,y) \right) \quad (1)$$

where A is the amplitude of the seasonal component, φ is the phase angle determining the timing when the seasonal harmonic amplitude reaches its maximum, k represents the harmonic modes ranging from 1 to T/2. T is the annual periodicity, set to 365 days, while t varies from 1 to 10 (years) × 365 days, corresponding to the current 10 full-year OISSS data record (2012 – 2021). The February 29 leap year day was excluded to simplify computation. The weekly OISSS was interpolated linearly to a daily resolution. Amplitude and phase are obtained from a least-squares fitting of the harmonic modes to the SSS daily time series.

2.3. The mixed-layer salinity budget

The mixed-layer salinity budget is performed to identify the primary mechanisms governing the connection between tropical and subtropical salinities. The mixed layer refers to the upper-ocean layer where physical parameters, such as temperature, salinity, and density, are considered well-mixed and therefore homogeneous from the surface down to the defined mixed-layer depth. By definition, salinity is constant within the mixed layer, and as such, SSS is treated as the mixed-layer salinity (MLS) in the analysis of the salinity budget equation. Following the approach of Mignot and Frankignoul (2003), the vertically integrated equation for MLS can be expressed as follows:

$$\frac{\partial S}{\partial t} = S_0(E-P) - \mathbf{U} \bullet \nabla S - (S - S_b)\Gamma(w_e)w_e + \kappa h \nabla^2 S \quad (2)$$

where S is salinity, S_0 the mean surface salinity, E evaporation, P precipitation, $\boldsymbol{U}$ the horizontal transport in the mixed layer, h the mixed-layer depth, w_e the entrainment velocity at depth $z = h$, and S_b the salinity chosen as the salinity 20 m below the mixed layer depth h. The Heaviside function Γ is introduced to represent the different effects of the entrainment ($\Gamma(w_e) = 1$) and detrainment ($\Gamma(w_e) = 0$) on the MLS. This means that the entrainment of subsurface stratified water influences the MLS when the mixed layer deepens, while the detrainment of the mixed-layer water into the subsurface does not alter the MLS when the mixed layer shoals (Kraus and Turner, 1967). The last term on the right-hand side of Eq.(2) is diffusion, where κ, the horizontal mixing coefficient, is set to 500 ms^{-2}.

The horizonal transport (**U**) is decomposed into the wind-driven Ekman component $\boldsymbol{U}_{EK}$ and the geostrophic component $\boldsymbol{U}_g$, which can be expressed as follows:

$$\boldsymbol{U}_{EK} = \frac{\boldsymbol{\tau} \times \boldsymbol{k}}{\rho f} \quad (3)$$

$$\boldsymbol{U}_g = \frac{hg\nabla\eta \times \boldsymbol{k}}{f} \quad (4)$$

where $\boldsymbol{\tau}$ denotes wind stress, g the gravity acceleration, f the Coriolis frequency, and η the sea surface elevation. The entrainment velocity w_e in Eq. (2) consists of vertical Ekman velocity w_{EK} and the h tendency:

$$w_e = w_{EK} + \left(\frac{\partial h}{\partial t} + \nabla \bullet h\boldsymbol{U}\right) = \frac{1}{\rho}\nabla \times \left(\frac{\boldsymbol{\tau}}{f}\right) + \left(\frac{\partial h}{\partial t} + \nabla \bullet h\boldsymbol{U}\right) \quad (5)$$

The Ekman vertical velocity w_{EK} corresponds to the upwelling/downwelling generated by the convergence/divergence of the horizontal Ekman transport. The h tendency term reflects the integrated effects of wind, surface buoyancy flux, and turbulent dissipation on the mixed-layer depth (Niiler and Kraus, 1977).

Each variable in Eq.(2) can be decomposed into a mean (denoted by an overbar) and the departure from the mean (denoted by a prime). The first order approximation for the MLS anomalies is expressed as:

$$\frac{\partial S'}{\partial t} \approx \frac{S_0(E'-P')}{\overline{h}} - \left(\overline{\mathbf{U}}_{EK} + \overline{\mathbf{U}}_g\right) \bullet \nabla S' - \left(\mathbf{U}'_{EK} + \mathbf{U}'_g\right) \bullet \nabla \overline{S} - \frac{(S-S_b)'\Gamma(w_e)w_e}{\overline{h}} + \kappa\nabla^2 S' \quad (6)$$

The left-hand-side denotes the rate of change of the MLS (or the MLS tendency). The seven terms on the right-hand side are: the effective surface freshwater flux forcing (FWF), advection of the MLS by mean Ekman currents (ADV_mEK), advection of the MLS by mean geostrophic currents (ADV_mGEO), advection of the MLS by anomalous Ekman currents (ADV_aEK), advection of the MLS by anomalous geostrophic currents (ADV_aGEO), entrainment/detrainment of the MLS through the base of the mixed layer (ADV_ENT), and lastly, horizontal mixing.

To compute the terms in Eq. (5), six datasets are required: S, P, E, τ, h,

and η. S is taken from the OISSS product, h is computed from the RG Argo monthly temperature and salinity products using a density criterion that sets h as the depth where density is 0.125 kg m^{-3} higher than the surface density (de Boyer Montegut et al., 2004). P is sourced from the Level 3 Daily 0.5° v3.2 product of the Global Precipitation Climatology Project (GPCP) (Huffman et al. 2020). E and τ are taken from the second generation, 0.25° gridded, satellite flux analysis produced by the Objectively Analyzed air-sea Fluxes (OAFlux) project (Yu 2023; in preparation). η has two components, the mean geostrophic component ($\overline{\boldsymbol{U}}_g$), which is computed using the time-averaged global mean sea surface height (Maximenko et al. 2009), and the geostrophic current anomalies ($\boldsymbol{U}_g^{'}$), which are computed from the altimeter sea surface

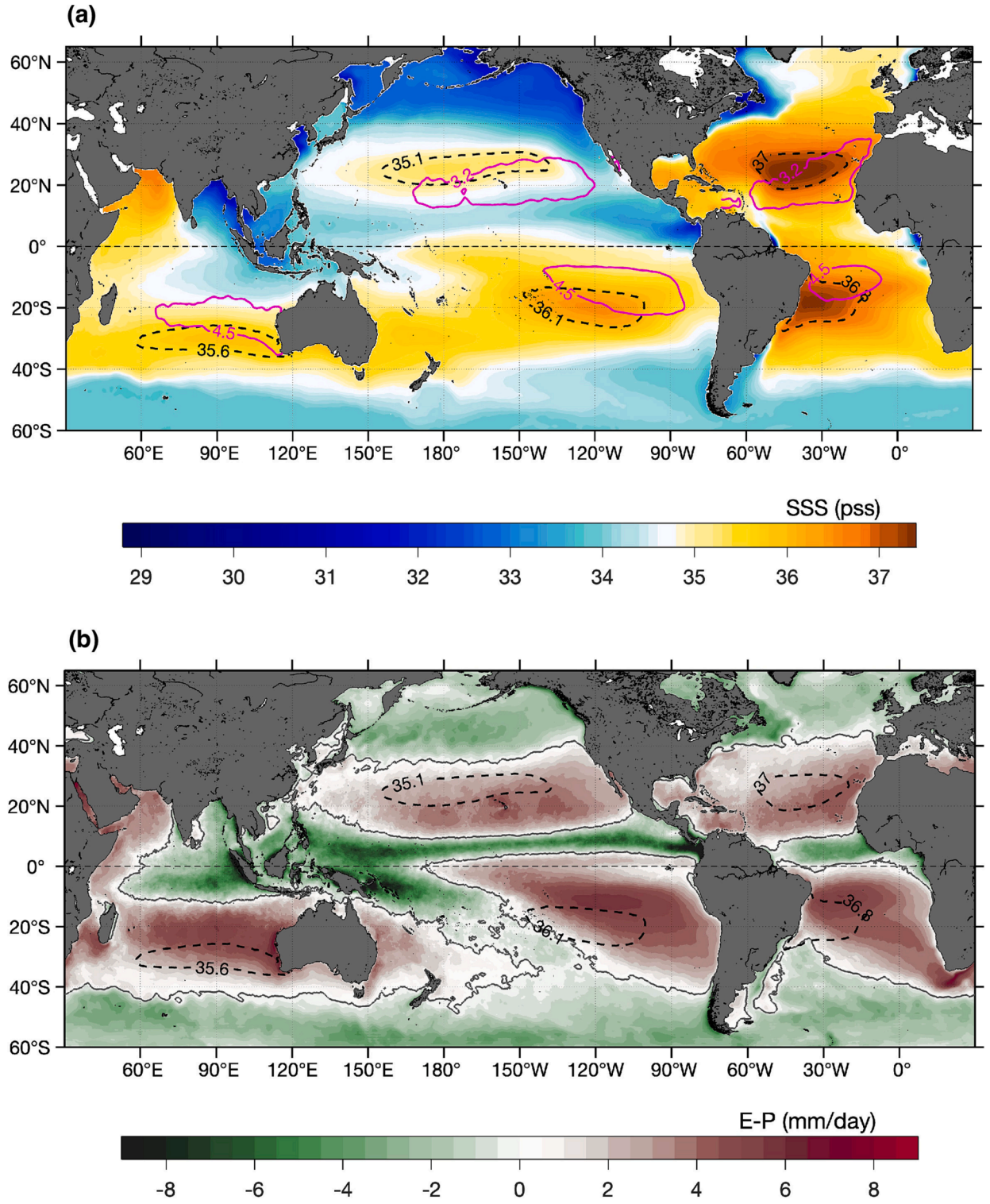

Fig. 1. (a) mean SSS and (b) mean E-P patterns averaged over the period of 2011–2021. In (a), the enclosed dashed black contours represent the *Smax* centers and the enclosed solid magenta contours represent the *(E–P)*max (or net evaporation) centers. In (b), the zero *E–P* isopleths are highlighted by solid black contours and the *Smax* centers are denoted by enclosed dashed black contours. (For interpretation of the references to color in this figure legend, the reader is referred to the web version of this article.)

height (https://www.aviso.altimetry.fr/).

The datasets have different spatial and temporal resolutions. The spatial resolution ranges from 0.25° (S, *E*, τ, and η), to 0.5° (*P*), and to 1° resolution (η), and the temporal resolution varies from daily (*P, E*, τ), to weekly (*S*), and to monthly (*h* and η). To ensure consistency in computing Eq. (6), the datasets of coarser resolution (e.g. *P* and *h*) were interpolated onto 0.25° grid boxes and the monthly datasets were implemented. The analysis focused on the 10 full years from January 2012 to December 2021, defined by the availability of the OISSS data record at the time of writing.

3. Results and discussion

3.1. SSS mean pattern and the annual harmonic mode

The marked contrast between the tropical low SSS and subtropical high SSS is clearly shown in the global mean SSS pattern averaged over the OISSS data record from January 2012 to December 2021 (Fig. 1). To highlight the geographic relationship between the subtropical *Smax* and the corresponding *(E–P)*max centers, the isohaline contour bounding the *Smax* center (thin dashed black contour) is drawn along with the isopleth contour bounding the (*E–P*)max.

center (thin solid magenta contour) for each open basin. The selected isohaline values (Table 1) are similar to those used in Gordon et al. (2015), Johnson et al. (2016), and Yu et al. (2021). Consistent with Gordon et al. (2015), the *Smax* centers in the North Pacific and Atlantic are situated near 26°N, the *Smax* centers in the South Pacific and Atlantic are near 18°S, and the *Smax* center in the South Indian Ocean is the farthest from the equator, at about 30°S. All of these *Smax* centers are displaced poleward relative to the (*E–P*)max centers.

Fig. 2 shows the spatial distribution of the annual amplitude and phase estimated from the harmonic analysis ($k = 1$ in Eq.(1)), with the *Smax* centers highlighted by the enclosed isohalines (black dashed contours). The annual harmonic amplitude describes the range of annual SSS variability (Fig. 2a). Consistent with previous studies (Yu et al. 2021 and references therein), substantial annual amplitudes (greater than0.3 pss) occur in areas affected by strong freshwater input, such as continental freshwater discharge and the ITCZ and SPCZ rainbands. In the subtropical *Smax* regions, annual amplitudes are generally weaker (~0.1 pss) at the center but noticeably larger (~0.2 pss) near the poleward edge of the *Smax* center.

The phase of annual harmonic represents the date of the year when the peak annual amplitude occurs. The peak amplitudes fall predominantly into two periods: March-April and September-October (Fig. 2b). In the mid latitudes (20–40°N/S) of the Pacific and Atlantic, the phases between the eastern and western basins differ by roughly six months. This east–west seesaw pattern is also observed in the South Pacific (Hanson et al. 2013) and Indian Oceans between latitudes of 20 – 35°S, but is much less apparent in the South Atlantic Ocean. Seager et al. (2003) suggested that the E-P flux in the western basin of the Northern Hemisphere is governed by the regional monsoonal circulation, while the E-P flux in the eastern basin is influenced by the subtropical high-pressure centers (Rodwell and Hoskins 2001). These two regulatory systems have contrasting annual cycles, which lead to opposing SSS annual patterns across the basin.

Table 1
Isohaline and E-P isopleth contours used to bound the *Smax* and *(E-P)*max centers in the five subtropical basins.

Variable	North Pacific	South Pacific	North Atlantic	South Atlantic	South Indian
Smax (pss)	35.1	36.1	37.0	36.8	35.6
*(E-P)*max (mm/day)	3.2	4.5	3.2	4.5	4.5

Of all features in Fig. 2, the zonal phase bands spanning the tropical-subtropical regions of the Pacific and Atlantic Oceans are of particular interest. Across the latitudes from the equatorward edge of the southern subtropical *Smax* at about 20°S to the equatorward edge of the northern subtropical *Smax* at around 20°N, there exist six zonal bands that have alternating phase shifts of six months. The phase band near the ITCZ is most pronounced, extending east–west across the basin. These zonal bands with opposite annual phases can also be identified in previous studies that used either in situ-based climatology (Boyer and Levitus 2002; Bingham et al. 2012) or satellite SSS observations (Yu et al. 2021). Collectively, they generate a captivating seasonal rhythm in the tropical-subtropical region.

It is worth noting that *Smax* center in the North Pacific and Atlantic comprises three phase signals rather than just one, with two being largely in phase and one out of phase. Taking the *Smax* in the North Pacific as an example. The center of *Smax* is dominated by SSS phases in March–April, while the north and south edges of *Smax* are reigned by two distinctive SSS phase bands, both in September–October. In the South Pacific and Atlantic, this three-band structure is also observed. It consists two March-April bands, one narrow centered around 15S and one wider stretching the southeast-northwest direction, and one September–October coming from the west of the basin, If one phase band represents the annual progression of a single physical process, then the three phase signals suggest that the annual cycle of *Smax* might be influenced by three different processes.

3.2. Poleward propagation of near-equatorial SSS anomalies

To investigate the tropical-subtropical seasonal rhythm in SSS, the evolution of climatological monthly SSS anomaly fields is shown. These monthly anomalies were constructed from the 10-year OISSS climatology with the annual-mean field subtracted. It is worth mentioning that the annual harmonic assumes the annual cycle to be a perfect cosine wave, while the climatological monthly-mean anomalies may contain signals that are not necessarily harmonic in nature. Nonetheless, Yu et al. (2021) showed that the annual harmonic is the predominant signal of the seasonal SSS cycle and accounts for more than 90 % of observed variances in the tropical-subtropical ocean. Hence, the evolution of climatological monthly anomalies should reflect the essence of annual SSS harmonic mode.

3.2.1. Tropical North Pacific

Fig. 3a-l shows the monthly SSS monthly anomaly evolution in the tropical North Pacific. Negative SSS anomalies indicate sea surface freshening, while positive anomalies represent sea surface salinification. Multiple zonal SSS anomaly bands with a slight northeast- southwest tilt can be seen, and the most prominent band is located near the ITCZ at approximately 5–10°N.

The ITCZ is known to migrate seasonally (Waliser and Gautier 1993), causing the wet and dry seasons at latitudes of 5–10°N. The wet season occurs during summer and early fall when the ITCZ shifts to its northernmost position, bringing increased rainfall to the region. The dry season takes place in winter and early spring when the ITCZ rainfall band is closer to the equator, resulting in drier conditions at latitudes of 5–10°N. Yu (2014; 2015) showed that during the wet season months in August-September, the Ekman convergence zone collocates with the ITCZ rainfall band (see Fig. 9 in Yu 2014). The convergence of the ITCZ-induced fresh surface water leads to the formation of a salinity minimum zone of 50–80 m deep under the ITCZ. After the formation, the Ekman transport, driven by tropical trade winds, advects the salinity minimum zone poleward away from its generation site. To track the progression of the ITCZ-induced SSS anomaly band from its first appearance to its final disappearance, two sequences of anomaly bands are numbered: the sequence of positive (saltier) anomaly bands is marked in red-circled numbers and the sequence of negative (fresher) anomaly bands are in blue-circled numbers. During the dry season in January-April, positive

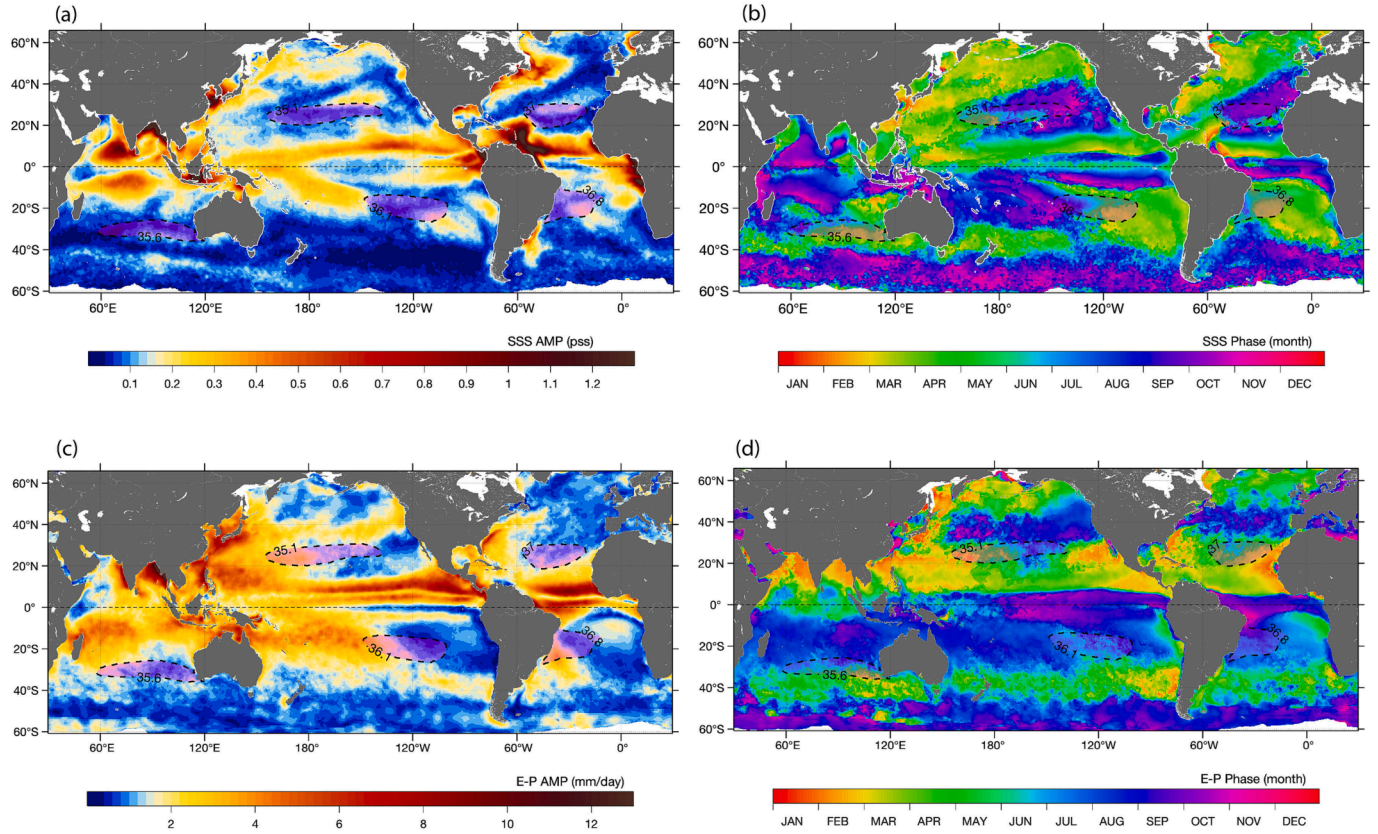

Fig. 2. Annual harmonic mode for SSS and E-P analyzed for the 10-year period from 2012 to 2021. (a) Amplitude and (b) phase for SSS. (c) amplitude and (d) phase for E-P. In all panels, the gray shaded area with dashed black outlines represents the Smax centers.

(saltier) SSS anomalies first appear around 5–8°N in January (Band ① in Fig. 3a), intensifying rapidly in February (Band ② in Fig. 3b), and reaching maximum intensity in March-April (Bands ③ and ④ in Fig. 3c-d). A subsequent northward migration follows (Bands ④ and ⑤ in Fig. 3d-e). By June (Band ⑥ in Fig. 3f), the entire anomaly band becomes weaker and more contracted as it moves northward, and the eastern portion of the band between 140°W and 90°W displays a northeastward tilt, clearly different from its previous southeastward orientation in January-March.

During the wet season in July-October, the positive anomaly band continues to weaken and contract while progressing further northward, reaching 12–14°N (Bands ⑦ and ⑧ in Fig. 3g-h). The latitudes of 5–8°N, where the positive anomaly band first appears in January, are now occupied by a negative SSS anomaly band (Bands ① and ② in Fig. 3g-h), coinciding with the northward displacement of the ITCZ rain band. The negative anomaly band reaches its seasonal maximum in September and October (Bands ③ and ④ in Fig. 3i-j). Meanwhile, the positive anomaly band shrinks to a narrow area with its center displaced near 20°N (Bands ⑨ and ⑩ in Fig. 3i-j), more than 10° of latitude northward from its original position in January-February. In the following months from November to December, the negative anomaly band weakens and moves northward (Bands ⑤ and ⑥ in Fig. 3k-l), while the positive anomaly band remains weak near 23°N (Bands ⑪ and ⑫ in Fig. 3k-l).

In January-February of the next year, the positive anomaly band from the previous cycle dissolves (Bands ⑬ and ⑭ in Fig. 3a-b), and a new positive SSS anomaly band starts to form (Bands ① and ② in Fig. 3a-b), with the same course of evolution repeating over another 12 months. The negative anomaly band continues its northward movement and contraction (Bands ⑦ and ⑧ in Fig. 3a-b), reaching 20°N in March-April (Bands ⑨ and ⑩ in Fig. 3c-d) and staying at the position for a couple of more months in May-June (Bands ⑪ and ⑫ in Fig. 3e-f) before disappearing near 23°N in July-August (Bands ⑬ and ⑭ in Fig. 3g-h). By then, a new negative SSS anomaly band forms (Bands ① and ② in Fig. 3g-h) and persists through another annual cycle. The northward advancement of the low sea surface salinity (SSS) band originating from the ITCZ region aligns with findings reported by Yu (2014; 2015) and others (Hasson et al. 2018; Melnichenko et al. 2019), but those studies were confined primarily to tropical areas spanning from 20°S to 20°N.

The SSS anomaly bands that originate from the 5°–10°N are distinguished by their extensive zonal scale across the entire basin, considerable magnitude, and their distinct sign reversal every six months. It is worth mentioning that there are significant negative SSS anomalies (<-1 pss) in the far eastern Pacific, specifically between 2°–5°N (Fig. 3a-c). This region is a central part of the eastern Pacific fresh pool (EPFP; Delcroix and Henin 1991; Alory et al. 2012), with mean SSS usually lower than 33 pss (Fig. 1). The EPFP is influenced by strong regional and seasonally varying ocean–atmosphere-land interactions, including ITCZ seasonal migration, monsoon rain, trade and gap winds, and strong currents, which result in significant seasonal and interannual variability in SSS (Alory et al. 2012; Giumbard et al. 2017). SSS anomalies in the region have a distinct seasonal pattern. For instance, from September to December (Fig. 3i-l), the EPFP's negative (fresh) SSS anomalies are confined between Panama's west coast and 85°W. At this time, the basin-scale negative SSS anomaly band, associated with the northernmost position of the ITCZ, is located at 5°–10°N. From January to April (Fig. 3a-d), the EPFP's negative SSS anomalies increase in intensify and extend westward to 95°W. In the west, they merge with the broader SSS anomaly band located just north of the equator, which is associated with the equatorward position of the ITCZ. In the south, they join with the negative SSS anomalies of the equatorial cold tongue during its warm season (Maes et al. 2014). As a result, the EPFP achieves its maximum freshness and largest spatial extent from January to April.

The SSS anomalies in the EPFP do not appear to directly contribute to the SSS anomaly band formed at 5°–10°N when the ITCZ is at its

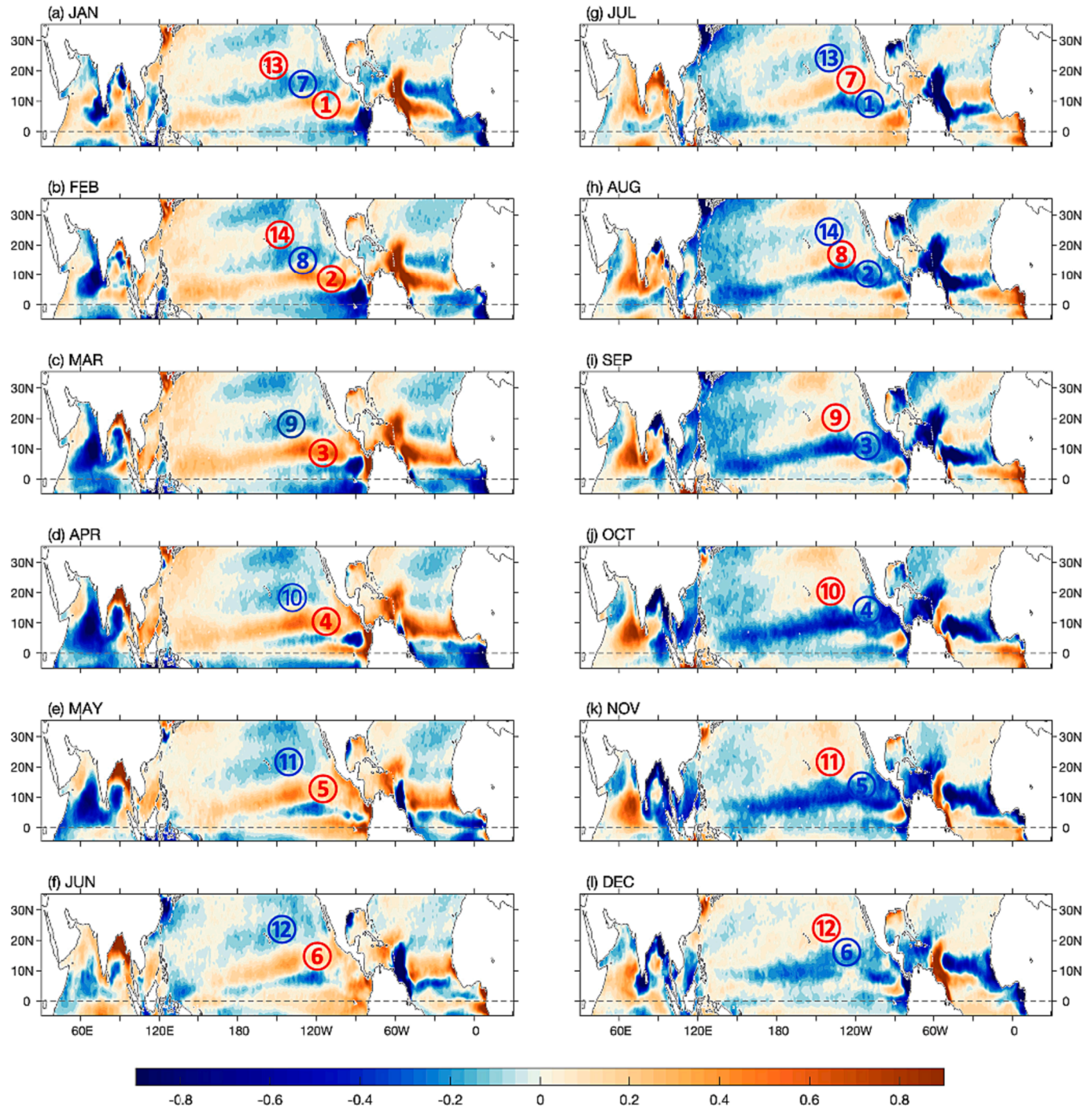

Fig. 3. Depiction of the monthly evolution of the SSS anomalies originating in the near-equatorial latitudes from January to December (a)-(i). In the North Pacific, the sequence of positive (negative) anomaly bands labeled by red-circled (blue-circled) numbers denotes the northward displacement of saltier (fresher) SSS anomalies. The monthly anomalies were relative to the 10-year (2012–2021) mean. (For interpretation of the references to color in this figure legend, the reader is referred to the web version of this article.)

strongest and northernmost position. Nonetheless, these anomalies may influence the development of the SSS anomaly bands in the tropical South Pacific, as shown in the subsequent sections.

3.2.2. *Tropical South Pacific*

Fig. 4a-l shows the annual progression of the SSS anomaly bands in the tropical South Pacific. Similar to the analysis of Fig. 3a-l, two sequences of anomaly bands are chosen: the positive (saltier) SSS anomaly bands are labeled by red-circled numbers and the negative (fresher) SSS anomaly bands are labeled by blue-circled numbers. It is noteworthy that, unlike the tropical North Pacific where the northward propagating anomaly bands originate from the latitudes of 5–10°N, the southward propagating anomaly bands initiate near the equator, on the southern flank of the eastern equatorial cold tongue region.

In January, the negative SSS anomaly band in the eastern equatorial Pacific consists of two regional features, as discussed in the previous subsection: the seasonal SSS freshening of the equatorial cold tongue during its warm season (Band ① in Fig. 4a) and the seasonal enhancement of the EPFP north of the equator (e.g. the enhanced low SSS anomalies on the northeast of Band ① in Fig. 4a). In February, the

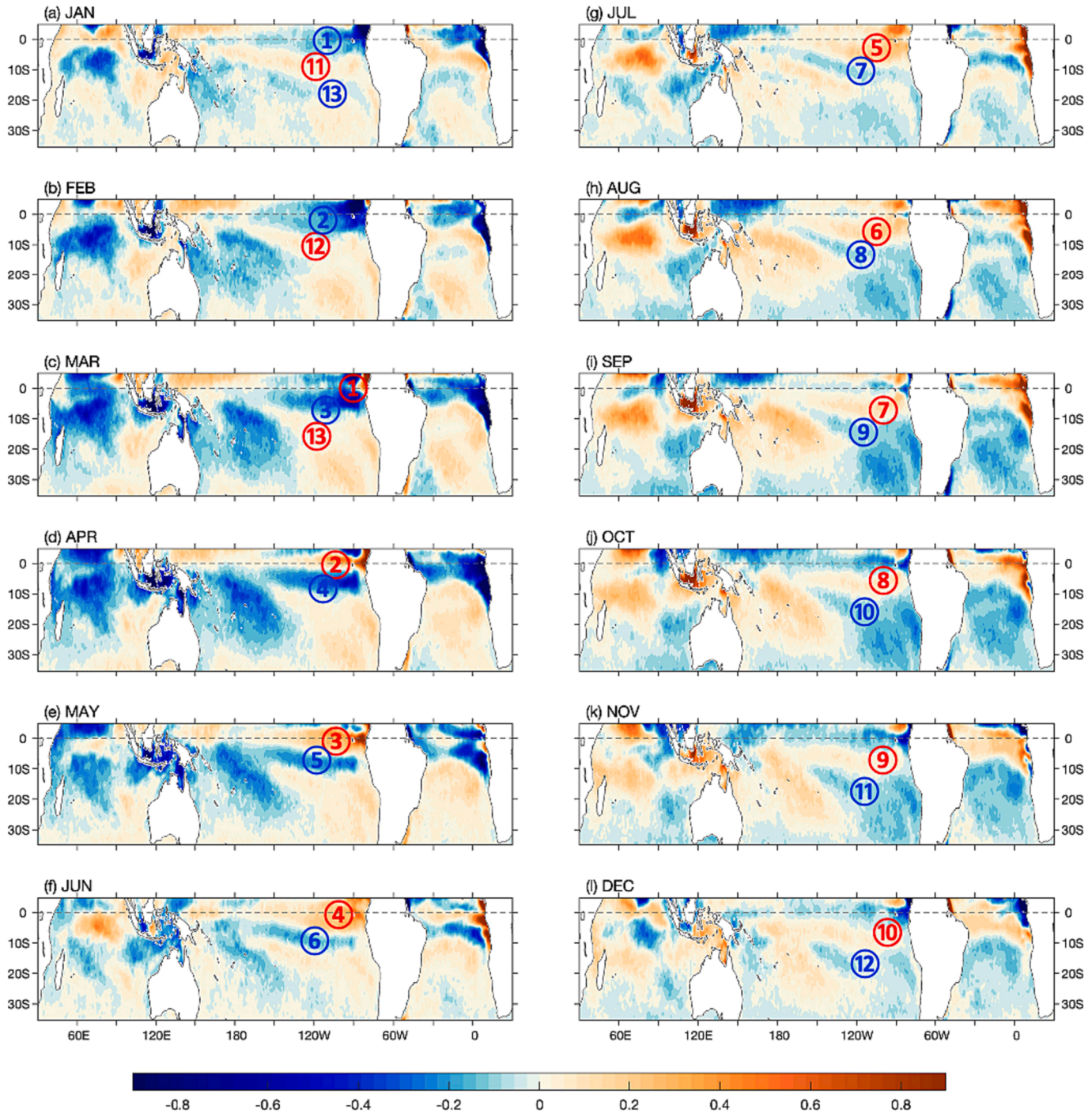

Fig. 4. Depiction of southward movement of SSS anomalies generated in the equatorial region and spreading across the southern tropical ocean from January to December (a)-(i). The sequence of positive (negative) anomaly bands labeled by red-circled (blue-circled) numbers denotes the southward displacement of saltier (fresher) SSS anomalies. The monthly anomalies were relative to the 10-year (2012–2021) mean. (For interpretation of the references to color in this figure legend, the reader is referred to the web version of this article.)

equatorial anomaly band intensifies and expands southward (Band ② in Fig. 4b). Martin and Stammer (2015) reported that the observed surface current pattern during this period suggests an influence of the EPFP on the occurrence of these low SSS anomalies.

By March and April, a negative SSS anomaly band with a magnitude of 0.5 pss is identifiable near 5°S, extending across the longitudinal span from 150°W to 90°W (Bands ③ and ④ in Fig. 4c-d). Moving into May to July, the band gradually weakens while shifting further southwestward, with its southernmost end reaching 10°S (Bands ⑤, ⑥, and ⑦ in Fig. 4e-g). Between August and November, the southward propagation of this band merges with a larger negative anomaly band that expands from a center near 20°S (Bands ⑧-⑪ in Fig. 4h-k). Finally, the band dissolves near 18°S in December-January (Band ⑫-⑬ in Fig. 4l-a), concluding its presence.

Positive anomalies start to appear in March, in the far eastern equatorial Pacific, just off the coast of Ecuador (Band ① in Fig. 4c), which is approximately three months following the emergence of the negative SSS anomalies. The evolution pattern of the positive anomaly band in the subsequent months is similar to that of the negative anomaly band. The positive anomaly band expands both westward and

southward (up to 5°S) from April to June (Bands ②, ③, and ④ in Fig. 4d-f). By July, the positive band in the eastern equatorial Pacific (150°W – 90°W) splits into two, with one on each side of the equator (Band ⑤ in Fig. 4g). The band south of the equator continues its southward movement over the subsequent six months, from August to January of the following year (Bands ⑥-⑪ in Fig. 4h-l and 4a), merging with the positive anomaly band from the south of 20°S before dissolving near 18°S in February (Band ⑫ in Fig. 4b).

3.2.3. *Subsurface*

To gain further understanding of the subsurface salinity structures associated with the SSS anomaly bands from their emergence to dissipation, Fig. 5a-l present the salinity monthly anomalies for the upper 150 m along the 140°W meridional section over a climatological year. These subsurface anomaly fields were constructed from the gridded RG Argo products using the same 10-year period (2012–2021). To be consistent with the SSS fields, red- and blue-circled numbers are assigned to the respective positive and negative anomaly sequence.

The subsurface salinity anomaly bands also exhibit a similar 14-month duration to the SSS anomaly bands, with a positive anomaly band initiating near 5°N in January (Band ① in Fig. 5a) and a negative anomaly band in July (Band ① in Fig. 5g). Consistent with Yu (2014; 2015), these anomalies of the salinity minimum zone are shallow, confined to a depth of 50 – 80 m below the surface. Once formed, the anomaly bands steadily progresses northward over the next several months until reaching approximately 23°N a year later (e.g., Band ⑬ in Fig. 5a or Band ⑬ in Fig. 5g). After that, the bands begin to dissipate (e.g., Band ⑭ in Fig. 4b or Band ⑭ in Fig. 5h). The positive anomaly band undergoes significant enhancement between 10 and 15°N as it migrates northward, reaching its maximum intensity and width in May (Band ⑤ in Fig. 5e). The negative anomaly band follows a similar evolution, with its maximum intensity and width reached in November (Band ⑤ in Fig. 5k). It is noteworthy that the salinity anomaly maxima at depths below the surface tend to occur approximately 1–2 months later than the anomaly maxima observed at the sea surface.

The salinity minimum zone in the tropical South Pacific is found to be slightly shallower than its northern counterpart. Martin and Stammer (2015) analyzed Argo profiles in the tropical South Pacific and confirmed the presence of the salinity minimum zone around 5°S, extending from the surface to a depth of approximately 30 m.

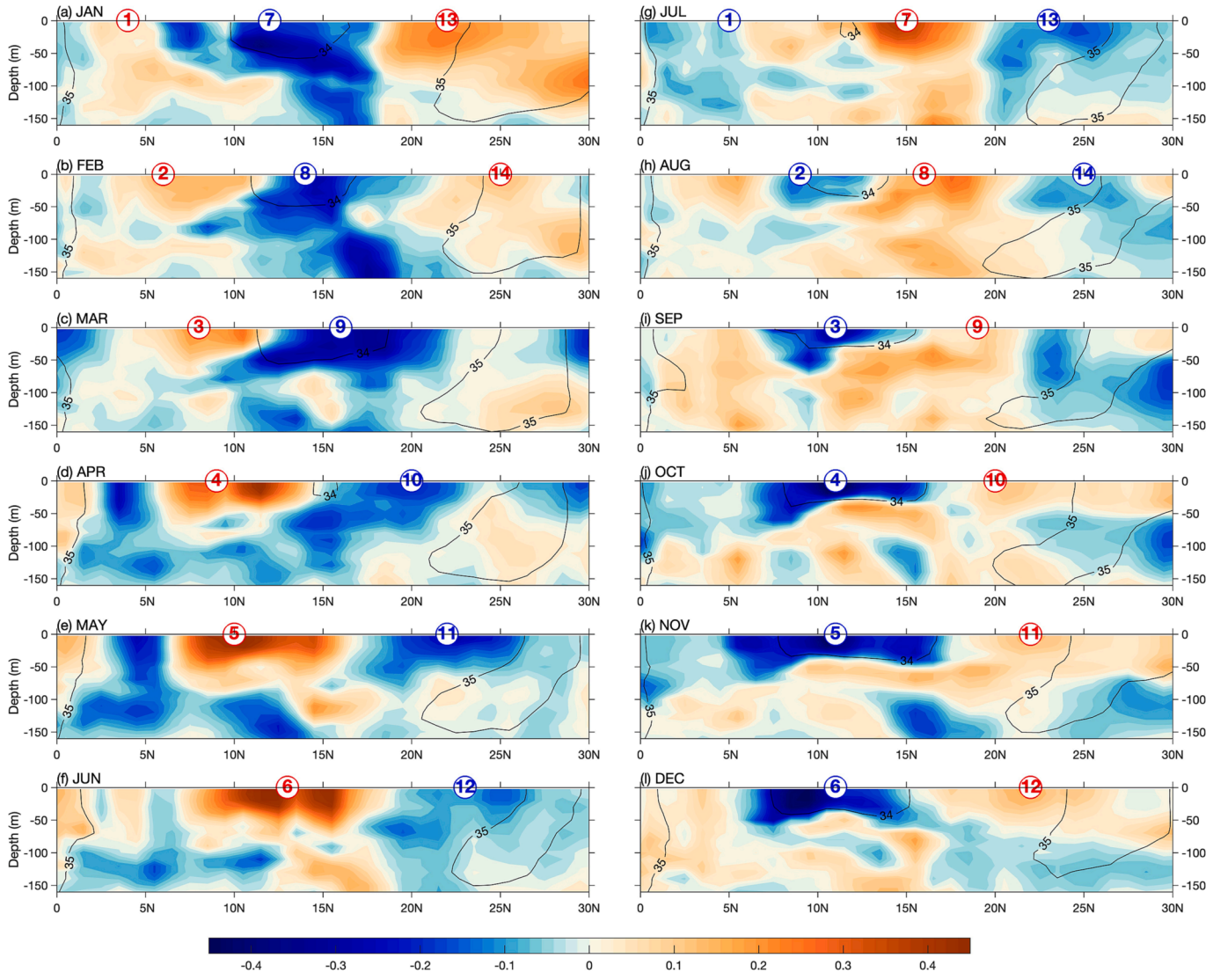

Fig. 5. Northward movement of the salinity anomalies in the upper 150 m along the 140°W meridional section in the north tropical Pacific ocean. Same as Fig. 3, the sequence of positive (negative) anomaly bands labeled by red-circled (blue-circled) numbers denotes the northward displacement of saltier (fresher) salinity anomalies. The monthly anomalies were relative to the 10-year (2012–2021) mean. (For interpretation of the references to color in this figure legend, the reader is referred to the web version of this article.)

Additionally, they found that the salinity minimum is accompanied by warmer water, with its maximum development observed during April, and the zone disappears during August. The propagation pattern is similar to that in the northern basins and is not shown here.

3.2.4. Time-latitude evolution

A Hovmöller diagram depicting the evolution of SSS anomalies averaged over the selected longitudes within the latitudinal range of 40°S and 40°N is constructed for all three basins (Fig. 6). The longitudinal sections are 140°W-100°W for the Pacific, 40°W-30°W for the Atlantic, and 70°E-90°E for the Indian Ocean. The isohaline contours that encircle the mean *Smax* in each basin are superimposed to indicate the *Smax* location. Two annual cycles are drawn to provide a fuller depiction of the poleward progression of SSS anomaly bands that have a duration of 12 – 14 months (Figs. 3–5).

The poleward propagation of SSS anomalies is evident in the Hovmöller diagram. These anomalies originate from near-equatorial latitudes and propagate to the equatorial flank of the *Smax* center in both the Northern and Southern Hemispheres. This feature has also been documented in previous studies (Yu 2014; 2015; Bingham et al. 2014; Melnichenko et al. 2019). In the northern tropical basins, the SSS anomaly bands (i.e., the blueish colors in Fig. 6) become more pronounced near 5–8°N during their northward progression from the equator. The SSS anomaly bands in the southern tropical basins are comparably weaker. The band in the South Indian Ocean extends beyond 25°S, which is the furthest among the three southern basins. The propagation speed of tropical salinity anomalies is estimated to be ~ 7 cm/s.

At mid latitudes poleward of *Smax*, a stationary wave-like structure is present, featuring alternating negative and positive patches occurring in roughly six-month successions. The *Smax* centers are located at or near the junction of these standing oscillation bands and the equatorial-originated poleward propagation bands. The evidence suggests that the subtropical *Smax* synchronizes with the near-equatorial *Smin* on seasonal timescales. Thus, the *Smin* and *Smax* in a basin are connected through a time lag.

3.3. Double ITCZs as the genesis of near-equatorial SSS anomalies

The genesis of the SSS anomalies north of the equator is relatively clear, as it is primarily associated with the formation of a salinity minimum zone at a depth of approximately 50–80 m beneath the sea surface (Yu 2015; Martins and Stammer 2015). This zone is created by the Ekman convergence of freshwater from the collocated ITCZ rainfall band during August and September (see Fig. 9 in Yu 2014). On the other hand, the cause of the SSS anomalies located south of the equator is not yet fully understood, as there are only a limited number of studies that have addressed this phenomenon. In this context, we present evidence (Fig. 7) to highlight that the southern ITCZ, which is a seasonal rainfall band located south of the equator around 3 – 10°S, is the source of the SSS anomalies in the south tropical Ocean.

Fig. 7a-c is a Hovmöller (time-latitude) diagram that displays the evolution of the equatorial rainfall monthly anomalies averaged over the longitudinal range of 140°W-100°W for the Pacific, 40°W-30°W for the Atlantic, and 70°E-90°E for the Indian Ocean. Two annual cycles are for the latitudinal range between 20°S and 20°N. In the eastern equatorial Pacific (Fig. 7a), a short-lived rainfall band emerges south of the equator, between 3° – 10°S, in January and intensifies during March and April. Concurrently, the predominant ITCZ north of the equator is weakest and also closest to the equator compared to other months of the year. This phenomenon, characterized by the simultaneous presence of twin ITCZs flanking the equator, is referred to as the double ITCZ (hereafter dITCZ) (Hubert et al.1969; Waliser and Gautier 1993; Zhang 2001; Halpern and Hung 2001; Liu and Xie 2002). The dITCZ is also

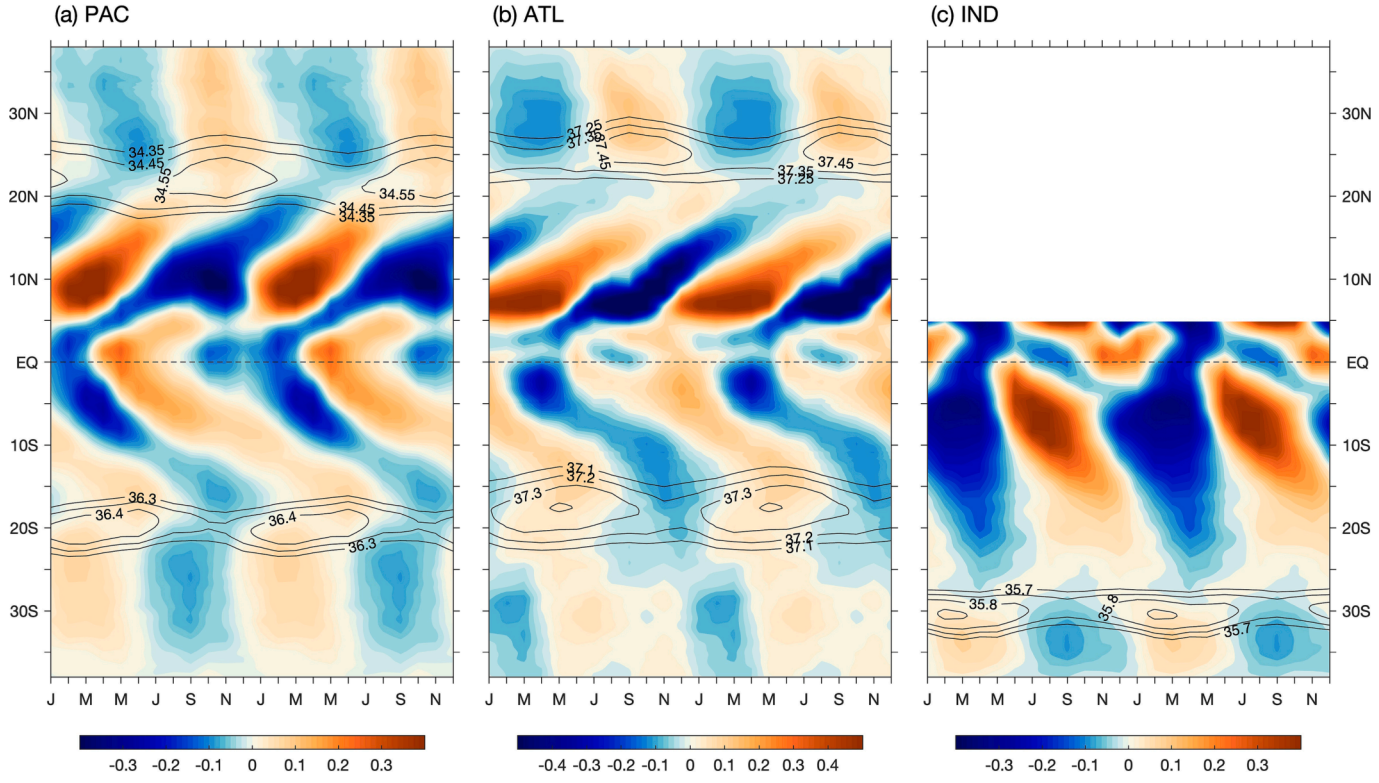

Fig. 6. Poleward progression of near-equatorial SSS anomalies averaged over the selected longitudes within the latitudinal range of 40°S to 40°N. (a) Pacific (averaged over 140°W – 100°W), (b) Atlantic (averaged over 40°W – 30°W), and (c) Indian Ocean (averaged over 70°E – 90°E). Two annual cycles are drawn. The isohaline contours encircling the mean *Smax* in each basin are superimposed. Positive anomalies denote higher SSS (saltier surface waters), while negative anomalies denote lower SSS (fresher surface waters).

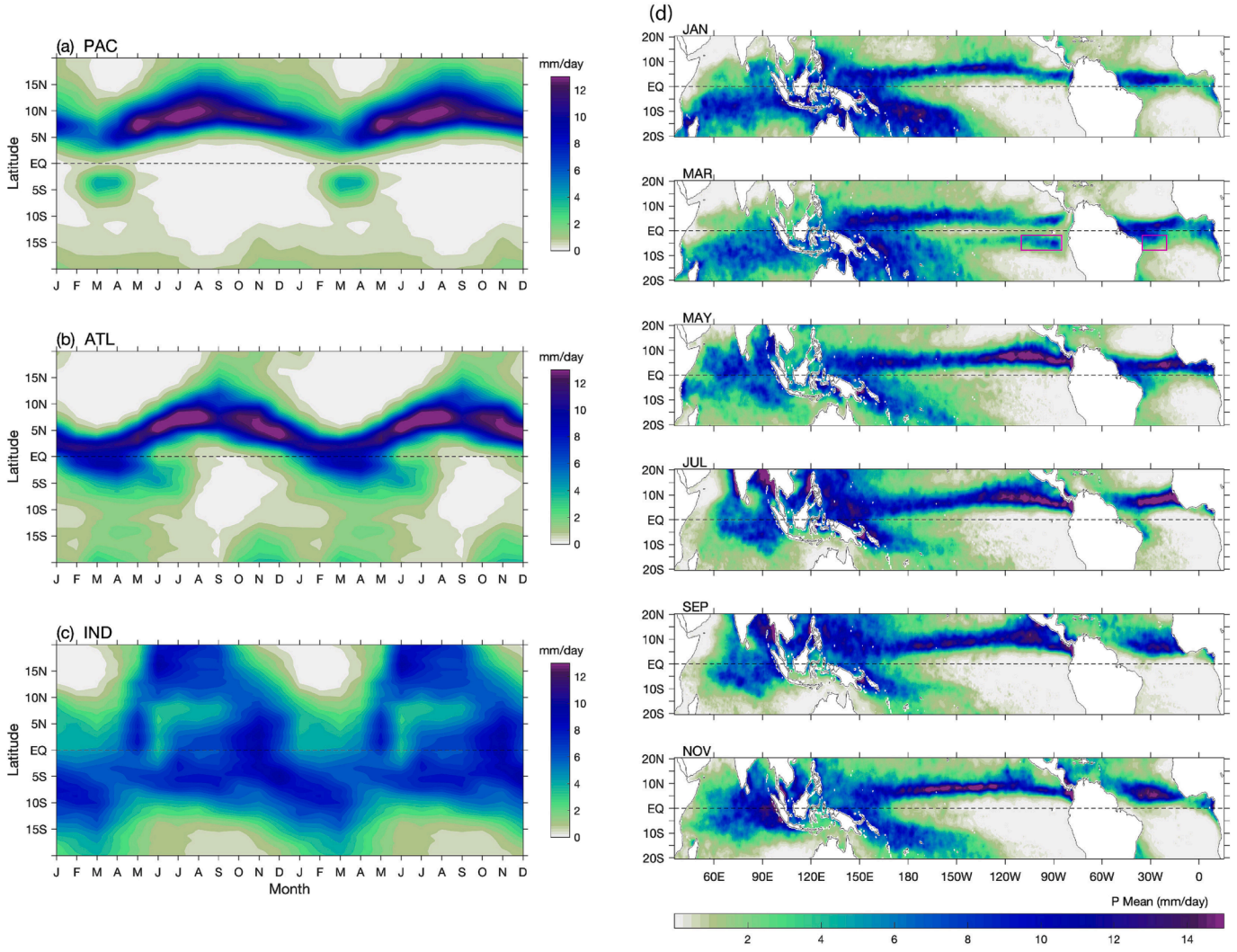

Fig. 7. Hovmöller (time-latitude) diagram depicting climatological annual rainfall cycle within the latitudinal range from 20°S to 20°N. The monthly mean GPCP precipitation was constructed for the 10-year period from 2012 to 2021. (a) Eastern Pacific (averaged over 140°W – 100°W) (b) Western Atlantic (averaged over 40°W – 30°W), and (c) Indian Ocean (averaged over 70°E – 90°E). (d) From top to bottom: Bimonthly variation of rainfall across tropical basins. The March panel highlights two red boxes, one in the Pacific (110°W–85°W, 8°S–2°S) and the other in the Atlantic basin (35°W–22°W, 8°S–2°S), to represent the areas used to construct time series plots in Fig. 8. The ITCZ bifurcates into two ITCZs north and south of the equator during boreal spring in the eastern Pacific and Atlantic, and during boral spring and fall (monsoon transitions) in the Indian Ocean. (For interpretation of the references to color in this figure legend, the reader is referred to the web version of this article.)

evident in the western equatorial Atlantic, albeit with slightly different characteristics (Fig. 7b). In this region, a bimodal pattern, most identifiable from May to July, evolves from an ITCZ rainband that was previously positioned on the equator between December and April. Lastly, in the central-eastern equatorial Indian Ocean (Fig. 7c), the dITCZ is less distinguishable and unlike that in the Pacific and Atlantic Oceans, the emergence of the northern ITCZ characterizes the dITCZ in the Indian Ocean (Waliser and Gautier 1993). The subsequent discussion will focus on the dITCZ pattern in the Pacific and Atlantic Oceans.

Compared to its northern counterpart, the southern ITCZ is generally weaker and highly dependent on the seasons. Two conditions have been identified as essential for the formation of the southern ITCZ: a narrow surface equatorial cold tongue caused by upwelling-favorable southeasterly trade winds, and a warm water band within 3° – 10°S that results from the annual procession of insolation (Lietzke et al. 2001; Halpern and Hung 2001; Masunaga and L'Ecuyer 2010). The meridional SST gradient resulting from this warm-cold contrast generates sufficiently large pressure gradient in the marine boundary layer, which drives a southward flow from the equator to converge with northward winds from the cooler Southern Ocean. This leads to the formation of the southern ITCZ over the SST warm band at 3° – 10°S and hence the rainfall in the region (Masunaga and L'Ecuyer 2010).

The bimonthly variations of tropical rainfall between 20°S and 20°N in Fig. 7d depict the spatial distribution of the double ITCZ rainfall bands over time. In January, the northern ITCZ is positioned close to the equator in both the eastern equatorial Pacific (120° – 80°W) and the western equatorial Atlantic (50° – 30°W). However, the subsequent development differs in the two regions. In the eastern equatorial Pacific, rainfall patches initially appear between 3° – 10°S in January, which intensify and expand westward by March, forming a significant rainfall band that extends up to 150°W and connects with the SPCZ. The southern ITCZ reaches a peak intensity of around 8 mm d^{-1}, which together with the northern ITCZ, forms a dITCZ on both sides of the equator. By May, the southern ITCZ mostly disappears, leaving only some remnants near 150°W in the western end. The characteristics of the dITCZ in the Pacific, as presented here, are consistent with those observed in previous studies (Waliser and Gautier 1993; Lietzke et al. 2001; Zhang 2001; Halpern and Hung 2001; Liu and Xie 2002).

In the western equatorial Atlantic, the southern ITCZ develops by the southward expansion of the southern edge of the ITCZ from January to March. By May, a weak and elongated rainfall band separates from the southern edge of the ITCZ and lingers around 3° – 10°S, while the northern ITCZ strengthens and moves northward. As July approaches, this band detaches from the northern ITCZ and contracts toward the west of 30°W, settling just off the northeast Brazilian coast. The maximum intensity of this band slightly exceeds 6 mm d^{-1}. As a result, the dITCZ in the Atlantic is mostly present during May-July (Fig. 7b), and the southern branch rapidly dissolves thereafter. Compared to the Pacific basin, the southern ITCZ in the Atlantic basin has a shorter zonal scale and a later formation. Grodsky and Carton (2003) analyzed the southern ITCZ in the Atlantic using satellite and ship-based observations for SST, winds, and rainfall. Although their analysis period (1998–2001) differs from the 10-year period (2012–2021) covered in this study, the pattern they derived for the southern ITCZ is similar to that shown in Fig. 7d.

The effects of southern ITCZ rainfall on local SSS have been examined in a few studies. Grodsky and Carton (2003) conducted a correlation analysis between satellite-derived rainfall data and in situ SSS measurements in the southwest Atlantic between 8° – 2°S. They found a seasonal freshening that coincided with the southern ITCZ rainfall, with an average reduction of 0.2 pss in SSS. Martins and Stammer (2015) investigated the role of rainfall variability in the seasonal occurrence of a low salinity zone around 8°-2°S from February to May/June using monthly observations over the period of 2005–2013. They showed that the salinity minimum zone of about 30 m deep was associated with higher temperatures and a shallow mixed layer depth, which together with the strong pycnocline in the region allows the weak precipitation to have a noticeable impact on SSS fields (Masunaga and L'Ecuyer 2010). They further showed that the response of the monthly-mean sea surface salinity (SSS) to the southern ITCZ rainfall was almost simultaneous, suggesting the predominance of freshwater forcing in the formation of the salinity minimum zone.

The connection between the southern ITCZ rainfall and SSS is examined here using 10-year monthly-mean time series of SSS and rainfall (*P*) constructed in two index regions: the southeast Pacific (145°–110°W, 8°–2°S) and the southwest Atlantic (50°–35°W, 8°–2°S), as shown in Fig. 7d (the March panel). Fig. 8 shows the two time series superimposed, with the 10-year mean removed from each dataset. Strong correlations between SSS and *P* are evident in both southern ITCZ index regions, with seasonal low (fresh) SSS anomalies corresponding to each seasonal high *P* event. The correlation coefficients in both basins are around −0.67, which is statistically significant at a 95 % confidence interval.

It is worth noting that the magnitude of surface freshening does not

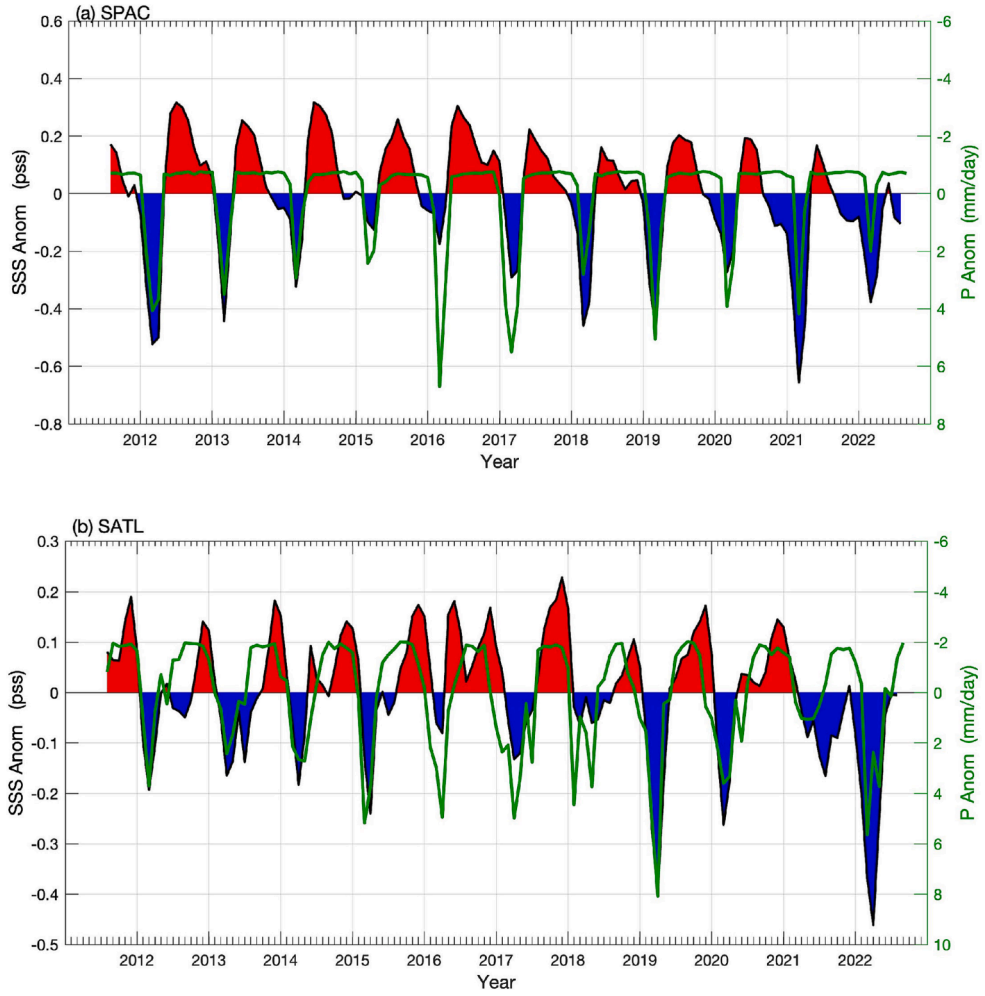

Fig. 8. Time series of SSS monthly anomalies averaged over selected areas within the southern ITCZ region. (a) South Pacific (110°W–85°W, 8°S–2°S), (b) South Atlantic (35°W–22°W, 8°S–2°S). These two areas are illustrated in the March panel of Fig. 7d. The superimposed green curve represents the rainfall time series averaged over the same areas. The SSS and precipitation anomalies are relative to their respective 10-year (2012–2021) mean. The y-axis on the left side of the panels represents the SSS anomalies and the y-axis on the right represents the precipitation anomalies. (For interpretation of the references to color in this figure legend, the reader is referred to the web version of this article.)

always correspond proportionally with high *P* anomalies. Additionally, the duration of the seasonal freshening may not overlap with that of the *P* anomalies. Martins and Stammer (2015) suggested that the low salinity water advected from the EPFP (Alory et al., 2012; Guimbard et al. 2017) could influence the SSS in the southeast Pacific index region. The likely intrusion of the low-salinity EPFP water from the north may explain the disparity in magnitude and duration between SSS and P. Over the 10-year analysis period, the peak low SSS anomalies in both the Pacific and Atlantic index regions occurred in March-April, with a mean of -0.31 ± 0.16 pss in the Pacific, and -0.16 ± 0.13 pss in the Atlantic.

3.4. Seasonal synchronization between Smin and Smax

Seasonal variations in the spatial extent of the five *Smax* centers are shown in Fig. 9a. Each *Smax* center is encircled by its respective isohalines in 12 climatological months, with each isohaline color-coded based on month. It can be seen that these *Smax* centers expand and contract in both zonal and meridional directions throughout the year. To see how these variations are related to seasonal changes of the low salinities near the equator, the annual cycles of *Smax* and *Smin* are depicted in Fig. 9b-f.

Unlike the *Smax* centers that can be enclosed by an isohaline, the *Smin* zones undergo annual formation and subsequent propagation (Fig. 2). Hence, a fixed area around the *Smin* formation latitudes is selected to characterize the annual variability of *Smin*. In Fig. 9a, these areas in the South Indian Ocean, North Pacific and Atlantic are denoted by blue-shaded rectangle boxes around the *Smin* locations (solid black lines; taken from Yu (2014; 2015)). The areas in the South Pacific and Atlantic are the same as those used in Fig. 8. There are a total of five pairs of *Smax* and *Smin*, one for each ocean basin. A numeric number is assigned to each of the selected *Smax* and *Smin* regions, starting from the South Indian Ocean. The first set of graph (the upper panel in Fig. 9c&e and lower panel in Fig. 9b,d&f) shows the monthly evolution of the zonally averaged SSS values over the enclosed *Smax* area. The second set (the lower panel in Fig. 9c&e and upper panel in Fig. 9b,d&f) shows the annual cycle of SSS (red solid line) averaged over the enclosed *Smax* areas and its comparison with the annual cycle of SSS (blue solid line) averaged over the selected rectangle areas around the *Smin* formation sites.

There are two noteworthy features in Fig. 9a-f. The first one is the relationship between the intensity and the meridional displacement of the *Smax* centers. Specifically, the *Smax* centers are equatorward displaced during December-January in the Northern Hemisphere (NH) and during June-July in the Southern Hemisphere (SH) (Fig. 9a). The intensity of the *Smax* centers changes accordingly: the SSS values of the *Smax* centers are lower (higher) when the centers are displaced equatorward (poleward). The second feature is the out-of-phase relationship in the annual cycles of *Smax* and *Smin*. In the North Pacific and Atlantic, the box-averaged SSS values (boxes 4 & 8) have a seasonal low in the late summer and fall (September-October) following the northward displacement of the ITCZ and a seasonal high in winter and early spring (March-April) following the equatorward displacement of the ITCZ. In the South Pacific and Atlantic, the annual cycle of the box-averaged SSS values (boxes 5 & 9) are predominated by a seasonal low in February-April when the southern ITCZ is present. In the South Indian Ocean, both seasonal low (March-April) and seasonal high (September-October) are featured in the annual cycle of the box-averaged SSS (box 1). Notably, the timing of the seasonal peaks for the SSS over the near-equatorial boxes (boxes 1, 4, 5, 8, & 9) is approximately six months opposite to that of SSS over the enclosed *Smax* areas (areas 2, 3, 6, 7, & 10) in the basin. It is important to mention that the seasonal progression of *Smin* in the tropical South Pacific and Atlantic is predominated by a pronounced low during its formation in the fall (March-April), but the seasonal high is less obvious. Nonetheless, the annual cycles of the SSS averaged over the *Smax* and *Smin* areas have a nearly perfect out-of-phase relationship.

The six-month time lag in the annual cycles between *Smin* and *Smax* appears to be associated with the time needed for the tropical SSS anomalies to propagate from their near-equatorial formation sites to the equatorward edges of the *Smax* centers from (Fig. 6). To further examine the lagged phase synchronization between these two SSS extrema, a phase-lagged correlation was conducted on the selected *Smin* and *Smax* location pairs for each basin (Fig. 9a). The correlation between each pair within the respective basin at various time lags, ranging from month 0 to month 12, is represented in Fig. 10. The results shows that the maximum correlation, reaching approximately 0.7, is observed at a six-month lag for all five pairs. Consistent with Fig. 9b-f, the seasonal variability of tropical and subtropical SSS has a nearly perfect six-month antiphase relationship.

Upon integrating Fig. 2b, 9, and 10, it becomes clear that the annual cycle of subtropical SSS maxima is phase locked to the tropical SSS minima. Specifically, the seasonal low of the *Smax centers* in the spring corresponds with the arrival of lower (fresher) SSS anomalies generated in the wet fall season when the ITCZ is displaced at its furthest poleward position (Fig. 7). In contrast, the seasonal high of the *Smax centers* in the fall aligns with the arrival of higher (saltier) SSS anomalies occurring during the dry spring season when the ITCZ is at its furthest equatorward position.

3.5. Ekman transport as oceanic pathway

The terms on the left-hand-side of the salinity budget equation (6) represent the atmospheric and oceanic contributions to changes in the mixed-layer salinity. These terms are analyzed to understand the primary mechanisms responsible for the observed seasonal synchronization between *Smin* and *Smax* centers. SSS is used here to represent the mixed-layer salinity, assuming a well-mixed upper layer. The horizontal mixing term is not displayed, as the effect is generally weak in the open ocean, especially away from western boundary currents and the equator (Roach et al. 2018).

3.5.1. Poleward propagation

To gain insight into the SSS propagating pattern shown in Fig. 6, we performed zonal averaging of the terms in Eq. (6) over the longitudinal span of 140°W-120°W, which is the same region used in Fig. 6a but for the northern basin between the equator and 40°N (Fig. 11). The observed salinity tendency, denoted by $\partial S'/\partial t$ OBS (Fig. 11a), is computed as the differences in SSS between two consecutive months using monthly-mean SSS observations. The salinity tendency calculated from summing the terms on the right-hand side of Eq. (6) is referred to as $\partial S'/\partial t$ SUM (Fig. 11b). The six contributing processes in Eq.(6) are also shown in Fig. 11c-h.

Two distinct sectors are featured in the $\partial S'/\partial t$ OBS and SUM patterns. One sector encompasses the latitudes from the equator to 26°N, characterized by SSS northward propagation. The other sector covers the latitudinal range between 26°–40°N, showing a standing alternation between positive and negative anomaly bands within one annual cycle. These two sectors intersect near 26°N. Among the six contributing terms to $\partial S'/\partial t$ SUM, three terms are predominant. The first term is the surface freshwater flux forcing (FWF; Fig. 11c), which leads to the ITCZ-induced SSS anomalies near 10°N and net evaporation-induced SSS anomalies near 35°N. Although these anomalies set the annual phase of $\partial S'/\partial t$, they appear as a stationary oscillation with no obvious propagation feature. The second term is the advection of mean SSS by anomalous Ekman transport (ADV_aEK; Fig. 11d). It influences primarily the salinity tendency in the subtropical latitudes of 20°–40°N. The third term is the advection of anomalous SSS by mean Ekman transport (ADV_mEK; Fig. 11e), which is the mechanism allowing the northward propagation of SSS anomalies from near the equator up to 35°N. The salinity advection by anomalous and mean geostrophic currents (Fig. 11f-g), ADV_AGEO and ADV_mGEO, respectively, also contribute to the northward propagation of SSS anomalies. However, the effect of

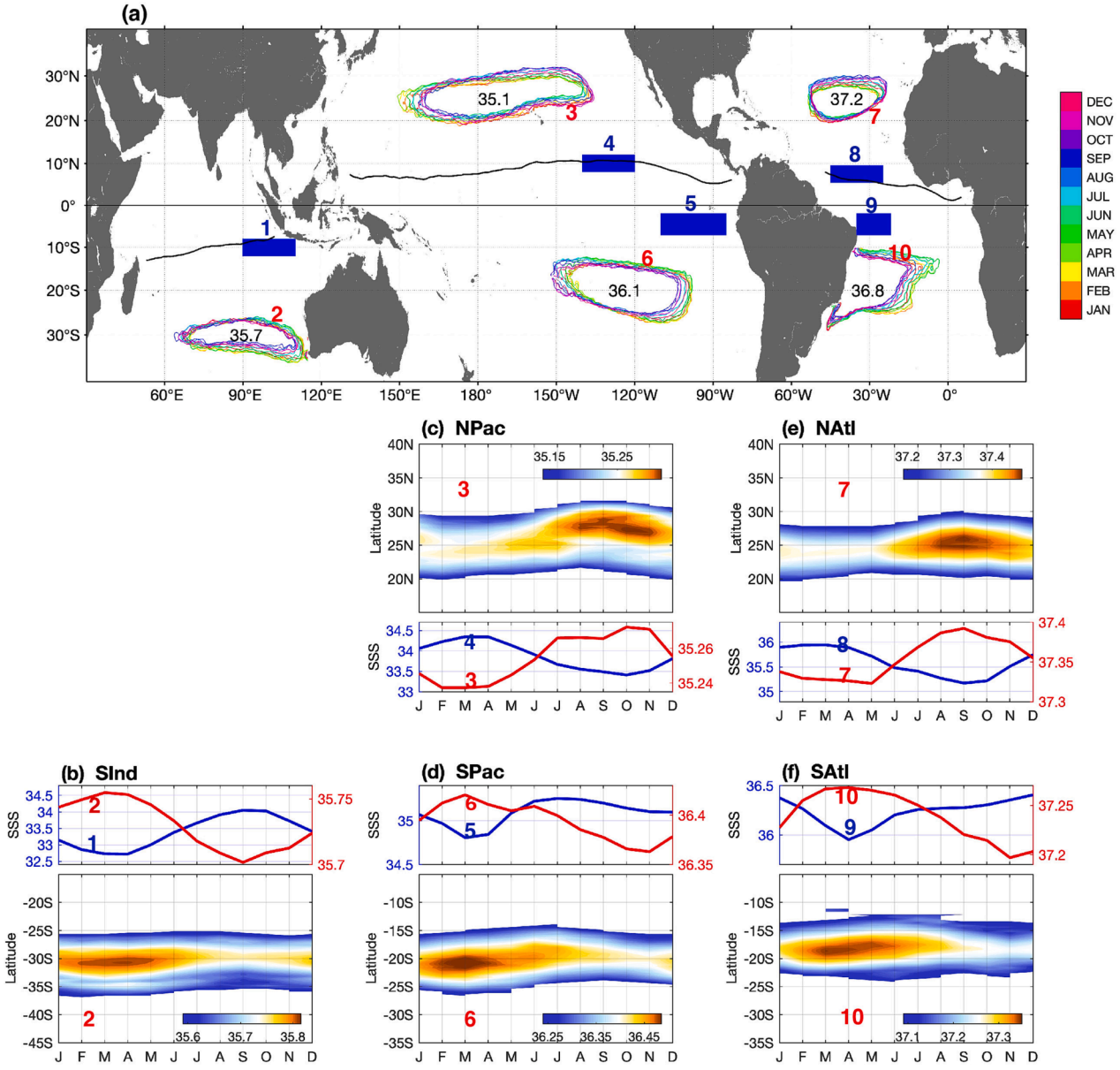

Fig. 9. Synchronization of the annual cycles in SSS over the selected Smin and Smax areas. (a) Monthly variations in the location of the isohaline contour encircling the Smax center in each basin, color-coded for each month. During the winter (summer) season of each hemisphere, the Smax centers are displaced toward (away from) the equator. Blue-shaded rectangle boxes near the Smin formation sites serve as the reference sites for SSS variability relating to Smin. These boxes in the North Pacific and Atlantic as well as the South Indian Ocean are within the mean Smin zones (solid black line), and the boxes in the South Pacific and Atlantic are the same as those used in Fig. 8. A numeric number is assigned to each of the selected Smax and Smin regions, starting from the South Indian Ocean to facilitate the depiction of the annual cycles of Smin and Smax in (b) South Indian Ocean, (c) North Pacific, (d) South Pacific, (e) North Atlantic, and (f) South Atlantic. (b)-(f) consists of two panels. One panel displays the monthly evolution of the zonally averaged SSS values over the enclosed Smax area. The other panel shows the annual cycles of SSS averaged over the enclosed Smax areas (red solid lines) and over the selected rectangle areas around the Smin formation sites (blue solid lines). (For interpretation of the references to color in this figure legend, the reader is referred to the web version of this article.)

ADV_aGEO is primarily confined within 10°N, although the impact of ADV_mGEO spans the entire basin. The vertical entrainment term (Fig. 11*h*), ADV_ENT, has a more significant impact on SSS increase in tropical latitudes during the late fall when the MLD deepens and entrains water from deeper layers.

The seasonal variations of $\partial S'/\partial t$ OBS and SUM along with the six contributing terms in Eq. (6) to the SSS tendency in the South Pacific between 40°S and the equator are shown in Fig. 12. All the terms are averaged over the longitudinal section from 140°W to 120°W. The $\partial S'/\partial t$ SUM captures well the propagating pattern shown in $\partial S'/\partial t$ OBS (Fig. 12a-b). Particularly, it indicates that ADV_mEK has a significant role in the southward propagation of SSS anomalies originating near the equator, while ADV_aEK governs the seasonal cycle of SSS in the subtropical region from 15°S and poleward. The two effects are similar to what Fig. 11 has shown for the North Pacific.

One major difference from the North Pacific is that the seasonal variations of $\partial S'/\partial t$ OBS near 10°S are predominantly controlled by ADV_mEK rather than FWF. The southern ITCZ rainfall occurs only from February to April and is absent for the rest of the year. The freshening tendency in $\partial S'/\partial t$ from July to March of next year is driven by ADV_mEK, with the low salinity waters likely sourced from the EPFP. As noted in sections 3.3.1–3.3.2, the EPFP waters from the north of the equator could intrude the southern equatorial Pacific through the cross-equatorial surface currents forced by gap winds (Martins and Stammer

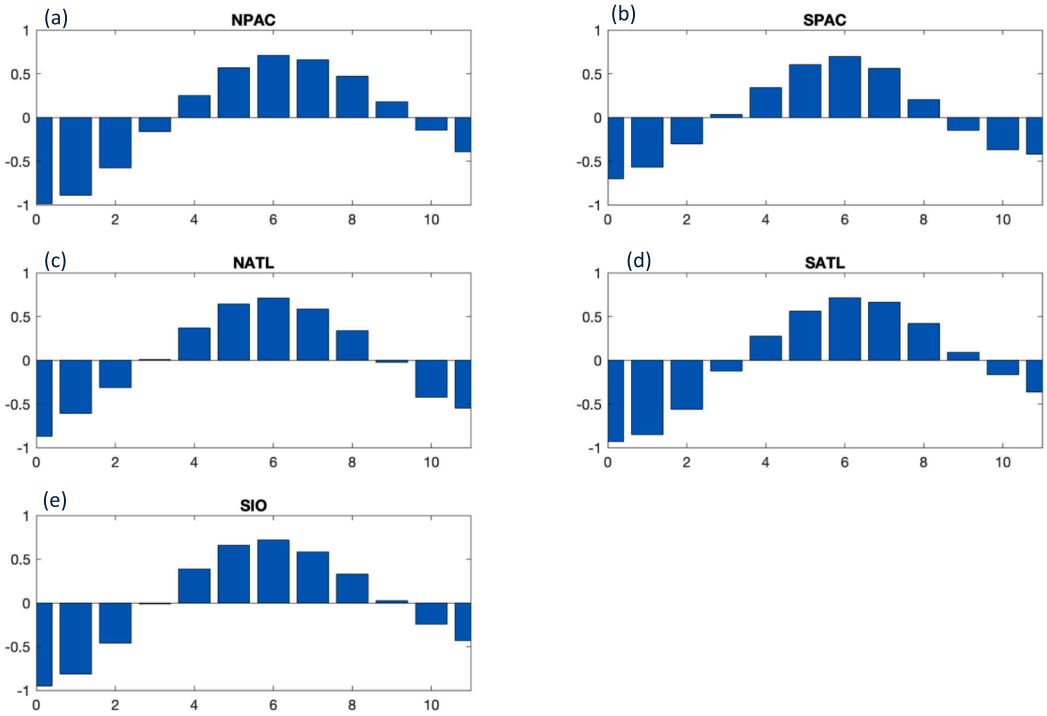

Fig. 10. Phase-lagged correlation between Smin and Smax in (a) North Pacific, (b) South Pacific, (c) North Atlantic, (d) South Atlantic, and (e) South Indian Ocean, analyzed with time lags ranging from 1 (month) to 11 (months). In each basin, the Smin location corresponds to the blue shaded box area highlighted in Fig. 9. The Smax location is in the vicinity of the numbers (2, 3, 6, 7, 10) indicated in Fig. 9. All basins exhibit a consistent six-month time lag, with Smin leading Smax. (For interpretation of the references to color in this figure legend, the reader is referred to the web version of this article.)

2015).

Fig. 12 showed that the horizontal salinity advection (including both Ekman and geostrophic) is an equal contributor as FWF to SSS variability south of the equator. The vertical entrainment is only relevant in March-May and serves to reduce the surface freshening. It is worth mentioning that there is a slight phase lag between $\partial S'/\partial t$ SUM and $\partial S'/\partial t$ OBS in region south of 20°S, where the surface freshening caused by ADV_aEK from April to October predominates the seasonal cycle of $\partial S'/\partial t$ SUM. This discrepancy implies that the sum of the terms considered in Eq. (6) cannot fully balance the salinity budget in the region. Martins and Stammer (2015) experienced the similar problem. The salinity budget imbalance may arise from several factors, including errors in data, the simplified representation of the equation, and the processes that cannot be resolved using observations, such as vertical salinity diffusivity and eddy-induced meridional salt flux.

In this study, the vertical physics is represented by the entrainment term in its linearized version (ADV_ENT), excluding vertical salinity diffusion, which greatly varies with vertical salinity gradient, mixing, and shear flow instability. Camara et al. (2015) highlighted the significant role of vertical salinity diffusion in their analysis of the salinity seasonal budget in the tropical Atlantic using an ocean general circulation model. They reported that vertical salinity diffusion is tightly phase-locked with near-surface stratification and works to reduce the vertical salinity gradient by upwelling saltier water from below. The extended seasonal freshening from April to October in $\partial S'/\partial t$ SUM (Fig. 12a) might be related to the inability to realistically represent the vertical salinity diffusion.

TIe importance of eddy-induced salt transport in shaping the mean salinity distribution within the subtropical salinity maximum regime has been investigated in several studies (Gordon and Giulivi 2014; Bryan and Bachman, 2015; Busecke et al. 2017; Qu et al. 2019). Bryan and Bachman (2015) pointed out that eddy-induced small-scale mixing is roughly equal in magnitude to the mixing provided by vertical diffusion acting on the climatological salinity distribution. They estimated that about half of the variance cascade between the large-scale and micro-scale occurs through the mesoscale eddy field. Qu et al. (2019) quantified meridional eddy salt transport in the three subtropical gyres in the Southern Hemisphere. Their results suggested that the eddy-induced salt flux can remove around19 % of the salt from the subtropical evaporative regime in the South Pacific, 16 % in the South Atlantic and up to 50 % in the South Indian Ocean. The absence of eddy-induced salt transport in Eq.(6) could be a significant factor affecting the salinity budget and causing the mismatched phase between $\partial S'/\partial t$ SUM and $\partial S'/\partial t$ OBS in region south of 20°S.

3.5.2. *Regime of Ekman dominance*

In Figs. 11-12, ADV_mEK stands as a dominant mechanism responsible for poleward advection of the SSS anomalies formed underneath the dITCZ. However, it should be noted that the governing mechanism for seasonal-to-interannual variability of SSS varies with locations (e.g. Mignot and Frankignoul 2003; Yu 2011; Camara et al. 2015). To identify the regime where ADV_mEK assumes a leading role, a covariance analysis was conducted. This method aligns closely with the approach employed in Yu (2011), but up-to-date, higher-resolution datasets are used in this study. The approach requires calculating the covariance of each term, labeled as *Xi,* with $\partial S'/\partial t$ OBS, and then normalizing it using the squared sum of all covariances. This metric is henceforth referred to as the normalized covariance (NCov) and can be expressed as follows:

$$\mathrm{NCov}(X_i) = \frac{\mathrm{Cov}\left(X_i, \frac{\partial S'}{\partial t}\mathrm{OBS}\right)}{\sqrt{\sum_{i=1}^{6}\mathrm{Cov}\left(X_i, \frac{\partial S'}{\partial t}\mathrm{OBS}\right)^2}} \times 100\% \quad (7)$$

The spatial pattern of NCov for each of the six terms in Eq. (6) is displayed in Fig. 13a-f, in which the location of *Smax* for each basin is superimposed to provide a contextual reference for the discussion. Positive NCov values indicate that the process, *Xi,* contributes to the SSS changes, while negative values indicate that the process, *Xi,* has an

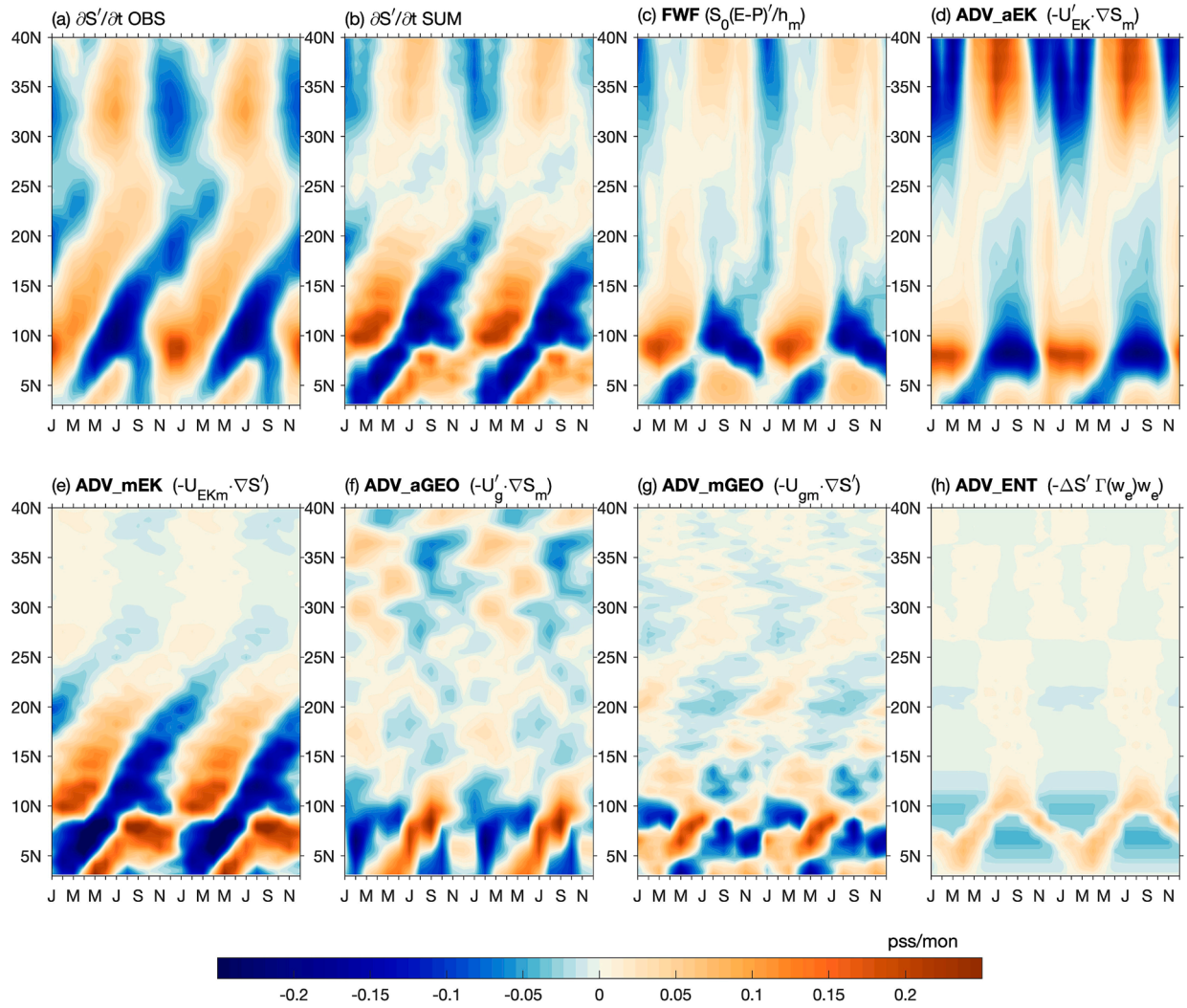

Fig. 11. Contributions of oceanic and atmospheric processes to salinity tendency diagnosed from budget equation (6). (a)-(h) Hovmöller diagram depicting the rate of seasonal salinity change (unit: pss/mo) averaged over the 140°W – 120°W longitudinal section in the North Pacific. (a) observed salinity tendency, (b) diagnosed salinity tendency, (c) freshwater flux forcing, (d) anomalous Ekman transport, I mean Ekman transport, (f) anomalous geostrophic transport, (g) mean geostrophic transport, and (h) vertical entrainment. In all panels, two annual cycles are drawn to enhance the representation of the movement of SSS anomaly bands.

opposite effect on the SSS changes. The six terms exhibit varying degrees of dominance across different regimes. Higher NCov(FWF) values (greater than80 %) (Fig. 13a) are typically observed in regions characterized by significant annual variations in E-P (Fig. 2c). The most notable regions exhibiting these patterns include: the western north tropical Pacific (5 – 30°N, 120 – 170°E) and Atlantic (15 – 30°N, 85 – 75°W), the eastern north tropical Pacific (5 – 20°N, 120 – 90°W) and Atlantic (5 – 15°N, 30 – 10°W), and the western south tropical Indian (25 – 5°S, 30 – 90°E) and Pacific (30 – 10°N, 150°E – 140°W). On the other hand, the presence of higher NCov values (greater than80 %) for the two Ekman transport terms, ADV_mEK and ADV_aEK (Fig. 13b-c), reveals intriguing disparities in spatial dominance. NCov(ADV_mEK) prominently dominates the tropical regions, extending from the vicinity of the equator to the equatorward edges of the subtropical Smax centers. By comparison, NCov(ADV_aEK) plays a primary role in the extratropical regions, specifically poleward of 15° north and south. Its positive contribution to the poleward section of each Smax center, coupled with its slight negative contribution to the equatorward section, is particularly noteworthy in the Pacific and Indian Oceans.

The spatial patterns of NCov for the two geostrophic transport terms, ADV_mGEO and ADV_aGEO, exhibit distinct characteristics. NCov (ADV_mGEO) tends to be predominantly negative in regions where NCov(ADV_mEK) is large positive, while its significance is not evident in other areas. Conversely, NCov(ADV_aGEO) is overwhelmingly dominant in the extratropics, especially in the latitudes poleward of the *Smax* center. Similar to NCov(ADV_aEK), NCov(ADV_aGEO) tends to have negative effect on the equatorward section of the *Smax* center, with the most pronounced impact in the southern basins. This suggests that the transport of mean salinity by seasonal Ekman and geostrophic currents acts to suppress the fresh anomalies that are generated by the ITCZ and advected poleward by mean Ekman currents. On a similar note, NCov (ADV_ENT) also tends to be predominantly negative in tropical regions where NCov(ADV_mEK) is large positive, emphasizing the important role of the subsurface salt entrainment in counterbalancing the surface freshening signal advected by mean Ekman currents.

To determine the dominant regime for each contribution to $\partial S'/\partial t$ OBS, the six NCov(*Xi*) values are ranked at each grid point. The highest value is regarded as the primary dominant contribution, while the second highest value represents the secondary dominant contribution. The primary dominant contribution regimes are depicted in Fig. 14a, with each regime color-coded for clarity. The pattern indicates that ADV_mEK and FWF are the two major contributors to $\partial S'/\partial t$ OBS in the tropical regions, spanning from near the equator to the equatorial edges of the subtropical Smax centers. FWF governs the SSS tendency in the western

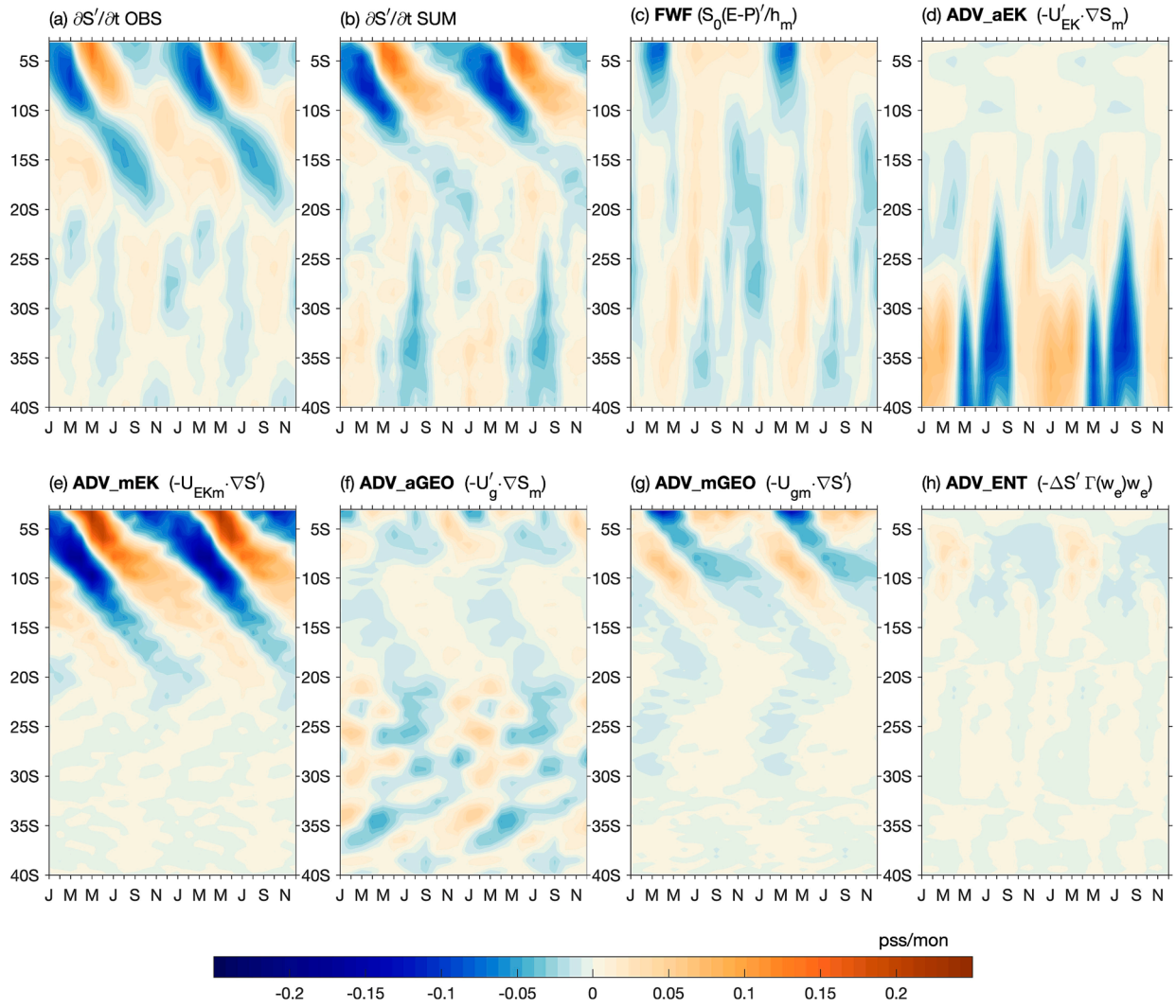

Fig. 12. Same as Fig. 11 but for the 140°W – 120°W section in the South Pacific.

and eastern portions of the basins, while ADV_mEK exerts dominant control over the central basins. Within the *Smax* centers, ADV_aEK emerges as the leading process in the North Pacific, North Atlantic and South Indian Oceans, whereas ADV_aGEO plays a significant role in the South Pacific and South Atlantic. The impact of ADV_aGEO is particularly pronounced in the extratropical region and the eastern tropical Indian Ocean.

The secondary dominant contribution regimes are depicted in Fig. 14b, using the same color coding as Fig. 14a. While the primary contributors are regarded as the driving force behind seasonal variability, the secondary contributors can be viewed as significant compensating processes that influence SSS variability. In areas characterized by the dITCZ, the salinity anomalies generated by FWF are primarily carried away by mean poleward Ekman transport. In the proximity of the *Smax* centers, ADV_ENT stands as the leading process to counterbalance the Ekman or geostrophic transport of the salinity anomalies from the ITCZ regions.

The dominant regimes were produced by Yu (2011) using climatological datasets with a coarser spatial resolution. This study employed contemporary datasets obtained from satellites, complemented by subsurface data from Argo floats. Despite these differences in data, the overall pattern is consistent between the two studies. The findings in Fig. 14a-b are in good agreement with an ocean general circulation model (OGCM) study by Camara et al. (2015). They showed that the seasonal variations of the MLS in the tropical Atlantic are comparably weaker in magnitude than the individual contributions from the FWF and oceanic processes, and that salinity anomalies induced by FWF are effectively attenuated by oceanic processes. In addition, the vertical diffusion coefficient was parameterized in the model using the Turbulent Kinetic Energy (TKE) scheme, which allows the diffusion coefficient to vary with factors such as stratification, vertical shear, winds, and buoyancy. By doing so, Camara et al. found that all oceanic processes, including vertical salinity diffusion, are all synchronized and phase-locked in their effects due to the influence of wind patterns.

3.6. Ekman versus geostrophic transport

Fig. 13b&d reveals two intriguing results. Firstly, ADV_mGEO has a sign opposite to ADV_mEK in the tropical region, which suggests a compensation between the mean Ekman and mean geostrophic advections of the ITCZ-induced SSS anomalies. Secondly, ADV_aGEO exhibits an overwhelming dominance in the extratropical regions, where ADV_aEK is relatively weak. A scaling analysis is conducted below to show that the relative importance of the Ekman and geostrophic currents varies with latitude.

The Ekman transport ($\boldsymbol{U_{EK}}$) induces water convergence and divergence within the Ekman layer, causing Ekman pumping (downward) or suction (upward) (Eqs. (3) & (5). This also generates a sloping ocean surface, creating pressure gradients that drive down-gradient flows. These flows, deflected by the Coriolis force, create geostrophic flows

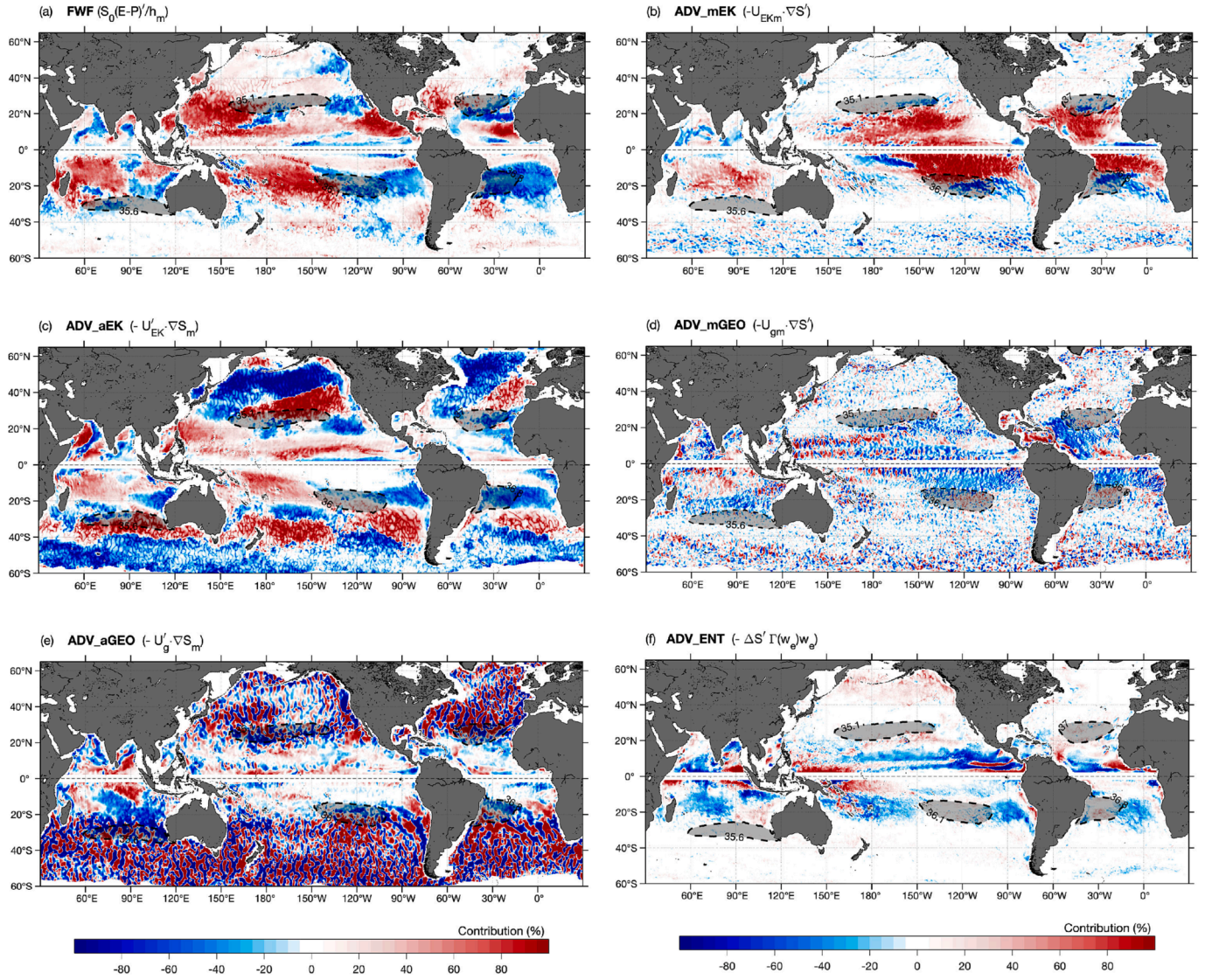

Fig. 13. Normalized covariance between the observed MLS tendency ($\partial S'/\partial t$ OBS) and the contributing process from (a) freshwater flux forcing, (b) mean Ekman advection, (c) anomalous Ekman advection, (d) mean geostrophic advectiI (e) anomalous geostrophic advection, and (f) vertical entrainment. The normalization is based on the scaling of the covariance by the sum of the six covariance matrices. Positive NCov values indicate that the specific process contributes to the SSS changes, while negative values indicate that the process has an opposite effect on the SSS changes. The location of the *Smax* center in each basin is denoted by the shaded area enclosed by a black dashed contour.

encircling higher-pressure centers. Interior geostrophic flows, resulting from Ekman transport-induced pumping/suction, are part of the wind-driven circulation.

When vertically integrating the entire water column and setting the surface and bottom vertical velocities to zero, the resultant equation represents the Sverdrup balance (Pedlosky 1996):

$$V_g = \frac{1}{\rho\beta}(\nabla \times \tau) \tag{8}$$

where β is the spatial derivative of $f = 2\Omega\sin\theta$, that is:

$$\beta = \frac{1}{R}\frac{\partial f}{\partial \theta} = \frac{2\Omega\cos\theta}{R} \tag{9}$$

where R is the Earth's radius and θ is the latitude. By combining Eqs. (3), (8)&(9), the relative significance of Ekman and geostrophic transports at different latitudes can be analyzed using the following scaling relationship

$$\frac{|V_g|}{|V_{EK}|} = O\left(\frac{f}{\beta L}\right) = \frac{R}{L}tan\theta \tag{10}$$

where the vertical bar represents the magnitude of the velocity, L is the length scale associated with the wind stress, which is significantly smaller than R. Assuming a value of $L = 1000$ km, the ratio in Eq. (10) is approximately 6.6 at 45°N/S where $\tan\theta = 1$ and exceeds 11 at 60°N/S. The increase in the ratio with latitude explains the dominance of ADV_aGEO at higher latitudes as suggested in Fig. 14a. On the other hand, in the equatorial region, a simple algebraic approximation of Eqs. (3)&(8) yields $V_g \approx -V_{EK}$, showing that the two meridional velocities are of similar magnitude but have opposite signs. This condition explains the compensatory effects between ADV_mGEO and ADV_mEK in the near-equatorial latitudes, as observed in Fig. 13b&d.

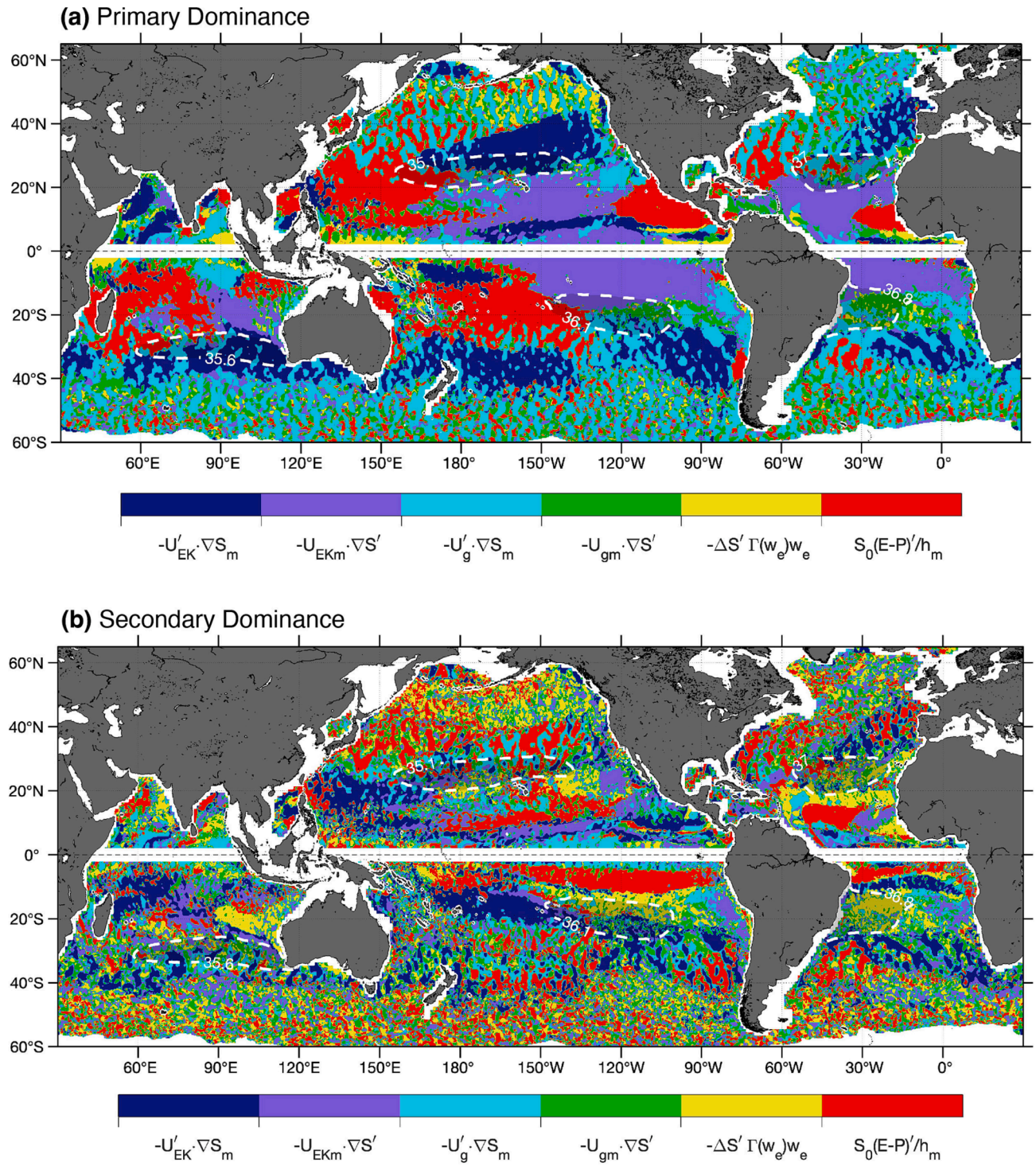

Fig. 14. Regime of (a) primary contribution and (b) secondary contribution to seasonal SSS changes from the six processes listed on the colorbar. The shaded area enclosed by white dashed contour represents a Smax center.

4. Discussion

4.1. Forcing constraints on the location of Smax

The analysis conducted thus far suggests that the lagged phase synchronization between the tropical *Smin* and subtropical *Smax* is primarily driven by the poleward Ekman transport of low SSS from the near-equatorial formation site to the subtropical *Smax* fringes. However, it is important to note that the Ekman transport undergoes a sign change in the horse latitudes around 30–35°N/S, where the trades and westerlies converge. This sign change indicates a transition in the direction of the Ekman transport, affecting the meridional extent of the tropical salinity influence. Fig. 15 shows this meridional extent using the streamline of the mean Ekman transport vector, with mean *Smax* centers superimposed as a reference. To facilitate the discussion, a convergence line is defined here as the location where meridional Ekman transport (V_{EK}) becomes zero and the transport on its north and south side changes signs. It can be seen that a convergence line is located around 30°N in

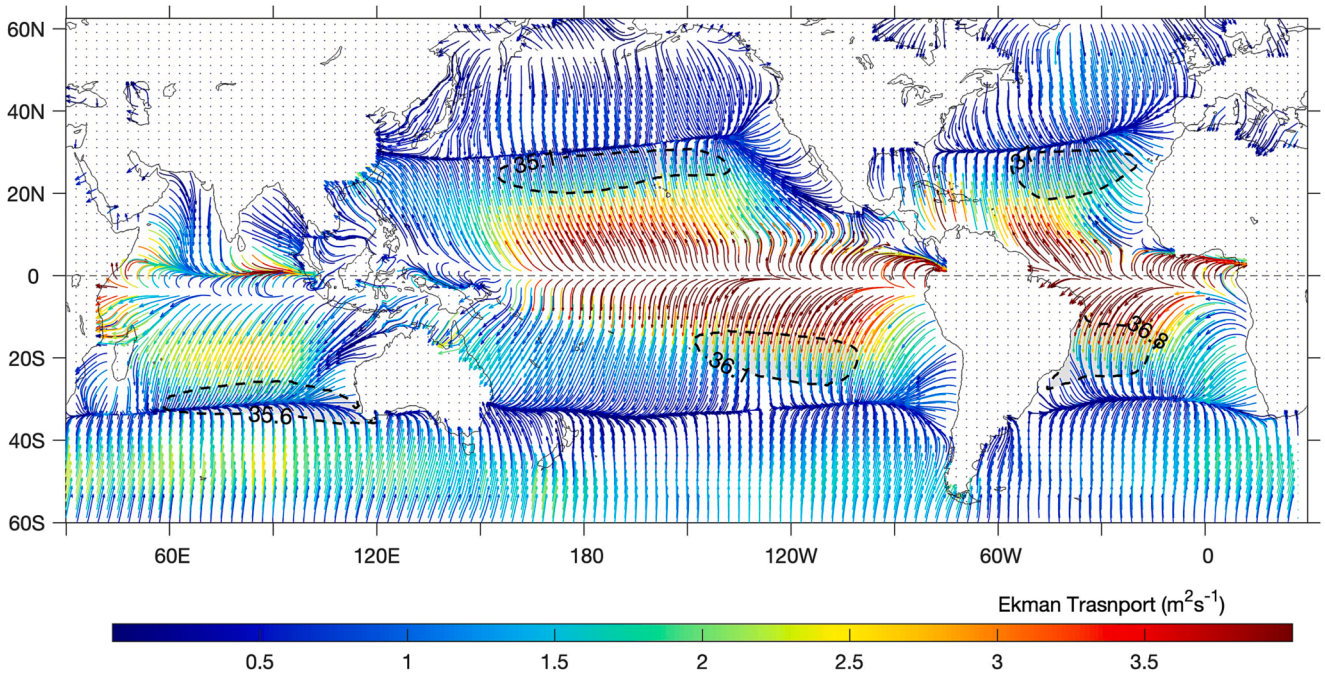

Fig. 15. Mean Ekman transport averaged over the period of 2012–2021. The direction of transport is denoted by arrows and the magnitude of the transport is scaled by colors. There is an Ekman convergence around 30°N in the Northern Hemisphere and near 35°S in the Southern Hemisphere. The shaded area enclosed by a dashed black contour represents the *Smax* center.

the NH and near 35°S in the SH.

The most remarkable revelation is the alignment between the poleward boundary of the *Smax* center and the Ekman convergence line in the North Pacific. The alignment indicates that the Ekman transport of tropical low-salinity anomalies plays a significant role in shaping the meridional displacement of the *Smax* center. Such close alignment is also prominent in the North Atlantic. In the South Pacific and South Atlantic, the *Smax* center falls within the poleward Ekman transport regime, with the poleward edge displaced equatorward from the corresponding Ekman convergence line. The South Indian is unique in that the line of zero Ekman transport coincides with the center of the *Smax*. One could argue that the isohalines bounding the *Smax* centers in the five open oceans (Gordon et al. 2015; Johnson et al. 2016; and Yu et al. 2021) are somewhat arbitrary in their selection. However, a change of the bounding isohaline does not change the alignment of the *Smax* center; it changes only the spatial expansion of the area containing the *Smax*, particularly in the zonal direction (see Fig. 2 in Gordon et al. 2015). Hence, the Ekman convergence line in the subtropical latitudes of ~30–35° north and south defines the meridional extent of the tropical low-salinity influence enabled by the poleward Ekman transport. To facilitate the discussion, the region confined by the Ekman convergence lines from ~ 35°S to ~ 30°N is referred to as the Ekman impact regime hereafter.

The displacement of the *Smax* center relative to net evaporation maxima has been widely studied (Walin 1982; Schanze et al. 2010; Zika et al. 2015; Ponte and Vinogradova 2016; Melzer and Subramanyam 2017). This study expands upon previous studies by establishing the internal synchronization of low–high salinities between the tropical and subtropical oceans. It adds to the existing body of research by showing that the *Smax* centers in all ocean basins are shaped by the Ekman poleward transport of the tropical low-salinity anomalies induced by the dITCZ (Fig. 15). Nonetheless, a critical question remains unanswered: What factors control the current locations of the *Smax* centers?

We argue that the poleward Ekman transport serves as an intrinsic mechanism in regulating the location of the *Smax*. This can be examined using the distance between the tropical *Smin* zone and the subtropical *Smax* center. According to Gordon et al. (2015), the *Smax* regime in the North Pacific and Atlantic spans between 20°N–30°N with a core at about 26°N. In the South Indian Ocean, the *Smax* falls between 26°S–32°S around a center near 30°S. In the South Pacific and Atlantic, the *Smax* regime is found between 15°S–22°S around a core at 18°S. Fig. 6 shows that the tropical *Smin* anomalies originate around 5–10°N in the North Pacific and Atlantic, 15–10°S in the South Indian Ocean, and near 2–5°S in the South Pacific and Atlantic. The distance between the *Smin* and *Smax* is surprisingly around 10–11 degrees of latitude in all basins, including the South Indian Ocean. Fig. 6 shows that the tropical salinity anomalies propagate at a speed of roughly 7 cm/s, similar to the estimate produced by Bingham et al. (2014) for the North Atlantic. At this speed, the tropical anomalies can cover a distance of roughly 10 degrees of latitude within six months, reaching the equatorial flanks of the *Smax* centers. If assuming the Ekman layer depth of 50 m, this traveling speed agrees perfectly with the Ekman current speed depicted in Fig. 15.

Nonetheless, the Ekman transport cannot be the only mechanism determining the location of a *Smax* center, as not all *Smax* centers have a good alignment with the location of the Ekman convergence line. The *E–P* flux is another important forcing, as the net evaporative freshwater flux acts as the primary source of salt, increasing the salinity of the surface waters, and is the fundamental basis for the existence of *Smax*. The influence of *E-P* is shown in Fig. 16, in which the net evaporation ($E > P$) zone (light blue shaded areas) and net precipitation ($P > E$) zone (green shaded areas) are superimposed onto the Ekman impact zone (red shaded areas). Notably, all *Smax* centers are well within the blue-shaded net evaporation zone. The *E-P* as a constraint for the location of a *Smax* is more evident in the SH. For instance, the southwest flank of the South Pacific *Smax* center near 25°S, 140°W falls right on the curvature of the zero line of *E-P*, and so does the southwest tip of the South Atlantic *Smax* center near 25°S, 45°W (see also Fig. 1b).

Apparently, there is a delicate balance between the high-salinity waters generated by E-P, the low-salinity waters brought by the Ekman transport in regulating the location of a *Smax* center. This is consistent with many previous studies, which have found that the salt accumulated under high evaporation is compensated primarily by Ekman low-salinity advection as the salt dissipated by mixing and

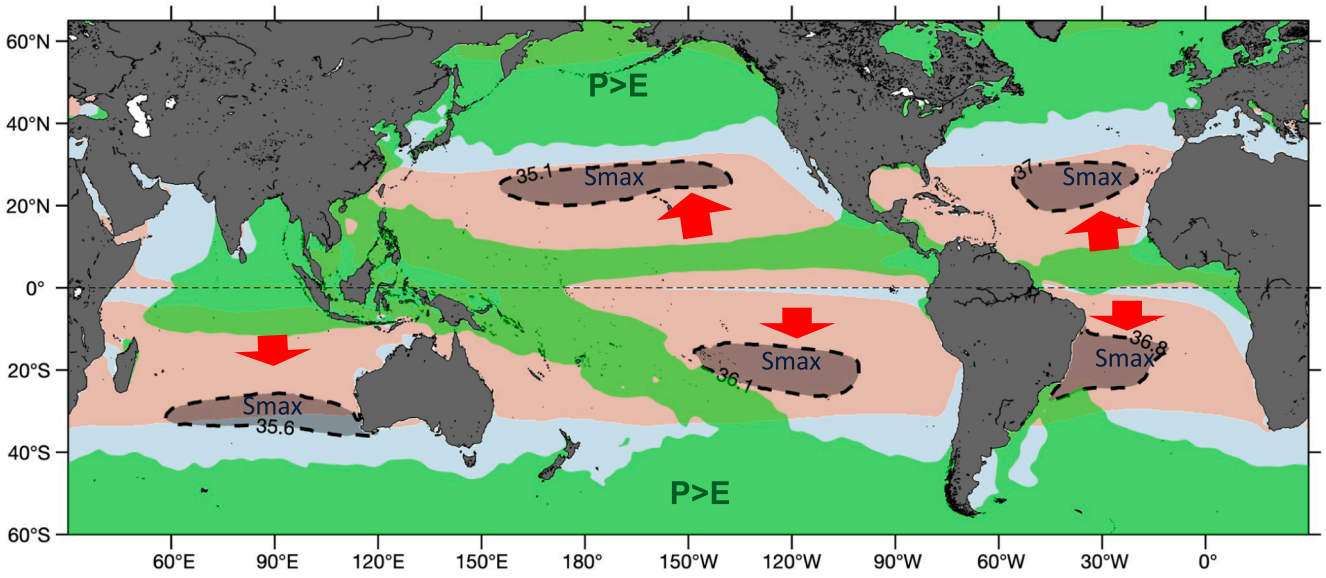

Fig. 16. Schematic diagram depicting the location of the subtropical Smax center (gray area enclosed by a dashed black contour) in relation to primary forcings. The Ekman poleward transport impact regime, highlighted in red, covers the region from 35S to 30 N, with the zone boundary defined by $V_{EK} = 0$ and bold arrow indicating the transport direction. The E-P regimes are superimposed, with the net precipitation regime (P > E) shaded in green and the net evaporation regime (E > P) shaded in light blue. Note that certain areas within the region between 30°N and 35°S are not shaded in red (indicating the absence of the Ekman impact regime) due to the meridional component not exhibiting a poleward direction in those specific areas (refer to Fig. 15). (For interpretation of the references to color in this figure legend, the reader is referred to the web version of this article.)

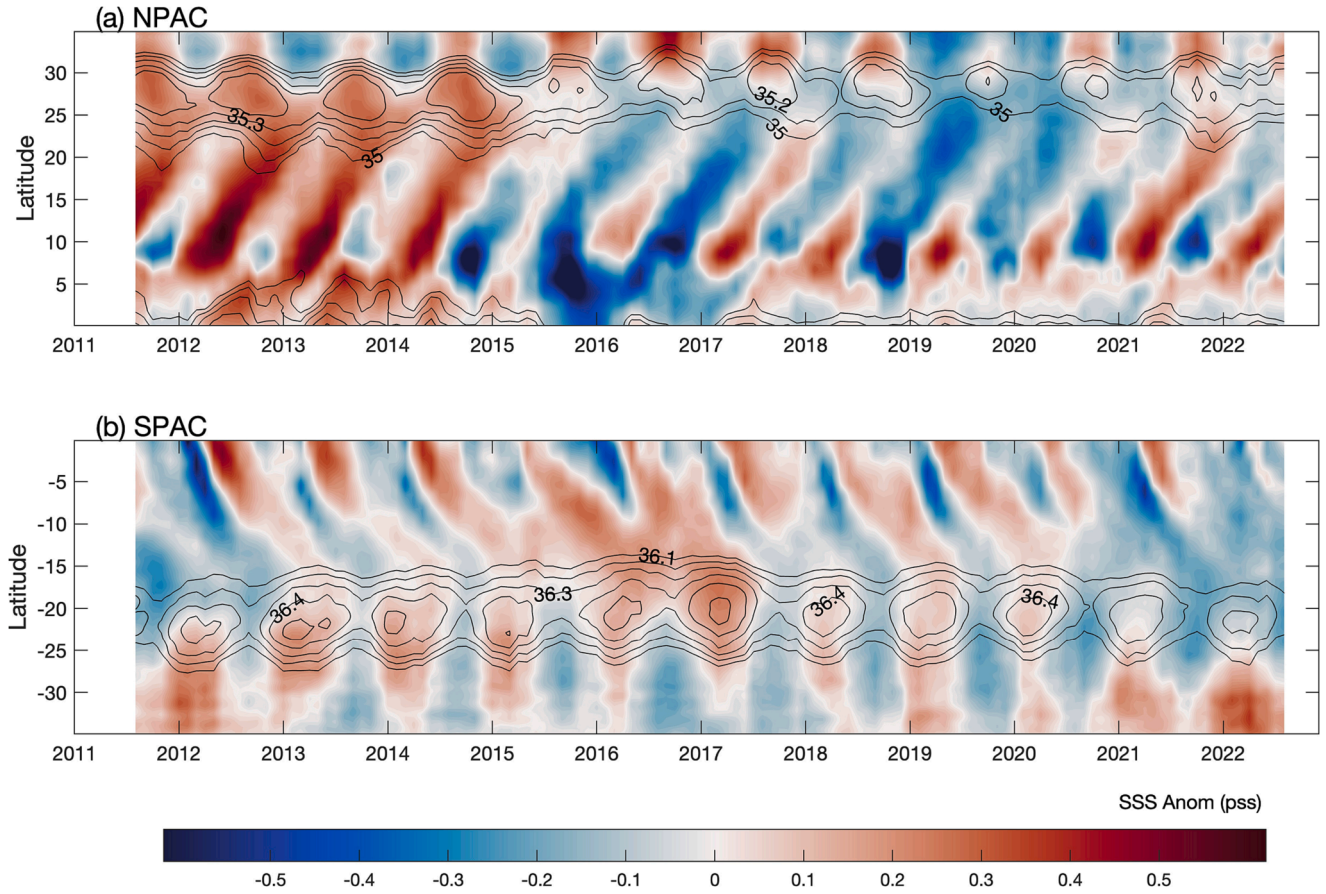

Fig. 17. Hovmöller diagram depicting the monthly evolution of SSS anomalies averaged over selected longitudes within the given latitudinal range. (a) North Pacific: 160°W-140°W, from the equator to 30°N, and (b) South Pacific, 120°W-100°W, from the equator to 30°S. The anomalies are relative to the 10-year (2012–2021) climatological mean. The superimposed black contour denotes the isohalines around the Smax center.

entrainment is not sufficient to balance the MLS budget, e.g. Qu et al. (2011, 2013) for the North Atlantic, Aubone et al. (2021) for the South Atlantic, Ren and Riser (2009) and Bingham et al. (2012) for the North Pacific, Hasson et al. (2013) for the South Pacific, and Wang et al. (2020) for the South Indian Ocean. Ponte and Vinogradova (2016) showed that ocean advection is manifested by the westward and poleward displacement of peak SSS regions relative to the *E-P* maxima. Putting all together, these studies support the viewpoint that the poleward displacement of *Smax* relative to net evaporation maxima is determined by the balance between salt production and the rate at which at which this salt can be compensated by ocean advection and diffusion (Walin 1982; Schanze et al. 2010; Zika et al. 2015; Ponte and Vinogradova 2016). Fig. 16 stresses that all these balance acts have to take place within the Ekman impact zone and the net evaporation zone, with the Ekman convergence line and the zero E-P line setting the uttermost boundary.

4.2. ENSO influence on the tropical-subtropical salinities

Hasson et al. (2018) reported a significant freshening anomaly (below – 0.5 pss) at 20°N in the tropical Pacific following the 2015–16 extreme El Niño event and attributed the emergence of this anomaly to the northward advection of the low-salinity anomalies induced near the equatorial latitudes by ENSO precipitation anomalies. The northward advection, which is dubbed as northward pathway by Hasson et al., is facilitated by the Ekman currents as well as the northward reflection of the North Equatorial Counter-current (NECC) into the westward-flowing North Equatorial Currents (NEC). They further showed that this northward displacement of SSS anomalies is not El Niño specific, even if the advection is enhanced during El Niño events. The findings of Hasson et al. indicate that the connectivity between the ITCZ-induced low-salinity anomalies could be a source of salinity variability in the subtropical high-salinity region on timescales beyond the seasonal cyclI.

The influence of the ENSO SSS anomalies outside of the equatorial region is examined in using the OISSS record from 2011 to 2021. Fig. 17a-b show the Hovmöller diagrams depicting the monthly evolution of zonally-averaged SSS anomalies over the selected longitudes in the North Pacific (160°W-140°W) and the South Pacific (120°W-100°W). The anomalies are relative to the 10-year (2012–2021) mean, revealing the change of the annual cycle of SSS during the satellite mission period. The influence of ENSO on the annual poleward advection of near-equatorial SSS anomalies is evident. In the tropical North Pacific (Fig. 17a), the effect is particularly pronounced during the 2014–2016 El Niño episode, at that time the northern ITCZ was located near 4°N, which was slightly northward compared to its typical Niño position on the equator (Zhong et al. 2019). The low-salinity anomalies (below –0.5 pss) were subsequently advected along the Ekman pathway, spreading the ENSO influence all the way up to 25°N, around the equatorial flank of the *Smax* center. Enahnced northward salinity advection was also observed during the 2018–2019 El Niño episode. Cumulatively, these anomalies caused a trend-like freshening in the tropical North Pacific over the decadal span of satellite salinity missions.

In the tropical South Pacific across the longitudes 120°W–100°W (Fig. 17b), the influence of ENSO on the annual southward propagation of the equatorial SSS anomalies is also prominent. It is noted that negative (fresh) SSS anomalies have increased considerably since 2020, which coincides with the prolonged persistence of La Niña that started in September 2020 and continued into 2023. The sea surface freshening occurred along the Ekman transport pathway, with the low-salinity anomalies reaching up to 30°S.

The linear trend map of the global SSS over the 10 full-year period (2012–2021) is shown in Fig. 18. The basin-wide surface freshening in the tropical North Pacific is one of the most remarkable features during this decade-long mission period. Additionally, surface freshening is also observed in the southeastern Pacific region between 15°S and 30°S. As shown in Fig. 17a-b, the poleward advection of near-equatorial low SSS anomalies along the Ekman pathways were abnormally active in recent ENSO episodes since 2014. Interestingly, when the mean Ekman convergence line ($V_{EK} = 0$) (represented by the green solid line) is superimposed, it becomes evident that the trend-like decadal freshening in both the tropical North and South Pacific is predominantly confined within the impact regime of Ekman transport. The precise alignment of the poleward edges of surface freshening trends with the mean Ekman convergence zone near 30°N is striking. This alignment affirms the

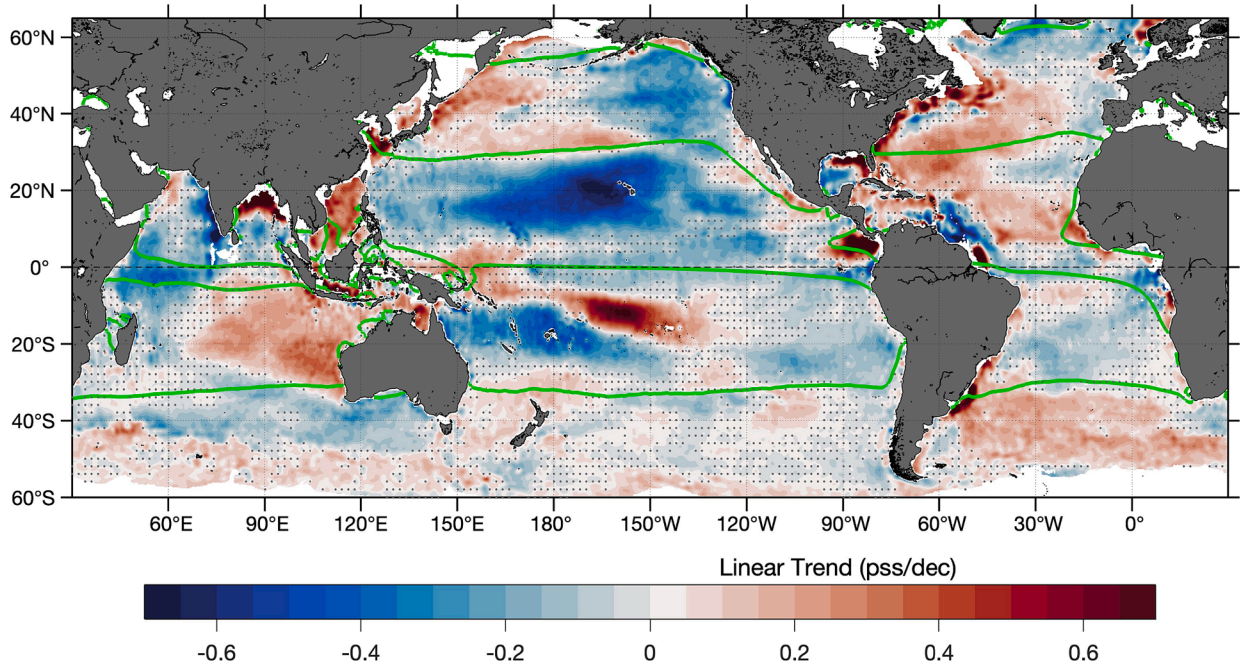

Fig. 18. Linear Trends for SSS over the 10-year period from 2012 to 2021. Positive (negative) trends indicate an increase (decrease) in SSS. The areas hatched by black dots denotes that trends that are not statistically significant at the 95 % confidence level. The thick green line denotes the mean Ekman convergence line. (For interpretation of the references to color in this figure legend, the reader is referred to the web version of this article.)

intrinsic connection between the tropical *Smin* and subtropical *Smax* regions and underscores the importance of the Ekman dynamics in governing the tropical-subtropical SSS variability on seasonal and longer timescales.

4.3. Link to the subtropical cells

The subtropical cells (STCs), first proposed by McCreary and Lu in 1994, are one of the important interaction mechanisms linking the equatorial ocean to the extratropical and subtropical regions. The STCs are shallow wind-driven overturning circulations in the upper 500 m, characterized by equatorward transport at subsurface level, and poleward transport in the surface layers, and closed by upwelling at the equator and subduction in the subtropics (Schott et al., 2004). Many studies suggest that the STCs act as "ocean tunnels" and influence the tropical–extratropical atmosphere–ocean interactions (Solomon 2010; Farneti et al., 2014) by either advecting subtropical temperature/salinity anomalies to the equator Gu & Philander, 1997), or by modulating the amount of subtropical waters transported to the equator (Kleeman et al., 1999; McPhaden & Zhang, 2002).

This study points out the connective nature of the tropical minimum and subtropical maximum SSS, showing that the poleward Ekman transport provides the essential oceanic pathway for this connection. It appears that this Ekman-enabled dynamical linkage between the tropical and subtropical salinities is in apparent association with one portion of the surface limb of the STCs: the poleward Ekman transport in the surface.

The surface limb of tICs includes the equatorial upwelling and poleward flow, while the lower limb consists of the subtropical subduction and equatorward flow. Many questions remain to be examined when integrating the observation-based finding of this study in the overarching framework of the STCs that was established from the tropical-subtropical temperature relationships (McCreary and Lu 1994). Unlike temperature, salinity is a tracer and does not interact directly with the atmospheric forcing. The only processes that can change salinity are mixing and entrainment. Therefore, the STCs are potentially an ocean memory for the change of the global water cycle through sequestering the subducted surface salinity anomalies in the pycnocline and reemerging these anomalies in the equatorial upwelling region in a decade later.

In the subtropical high SSS regions, the winter-time subduction of the salty surface waters leads to the formation of a distinct salinity maximum with a core at the depth of 100 – 150 m. This subsurface salinity maximum water is known as Subtropical Underwater (STUW) (O'Connor et al. 2005; Shcherbina et al. 2015; Yu et al. 2018). Once formed, the STUW is exported equatorward along the lower limb of the STCs (Fine et al. 2001; Busecke et al. 2014). Using model simulations, Qu and Gao (2017) studied the resurfacing of South Pacific Tropical Water (SPTW) in the equatorial Pacific and its variability associated with ENSO. Their results demonstrate a high correlation of both the volume and barycenter of the resurfacing SPTW with ENSO indices. The resurfacing SPTW reaches its minimum volume and easternmost position during El Niño years and maximum volume and westernmost position during La Niña years.

While the subduction of subtropical high salinities and the subsequent advection through the lower limb of the STCs appear to be better described, the surface limb, where the pycnocline water upwelled in the equatorial region flows poleward driven by Ekman transport, is less known. With this study, the dynamical linkage between the tropical and subtropical salinities established from observations helps fill the knowledge gap for the processes relating to the surface limb. Still, many questions remain open, including but not limited to, how the low surface salinities formed under the dITCZ interact with or is influenced by the upwelled water properties at the equator; how the tropical low salinities are transformed after going through the net evaporation zone; and what water cycle signals are carried by the subducted water masses, etc. Evidently, further work is needed to explore these issues.

5. Summary

This study investigated the connective nature of the tropical *Smin* and the subtropical *Smax* and revealed that the poleward Ekman advection of SSS anomalies originating near the equatorial latitudes serves as an essential oceanic pathway for this tropical-subtropical connection. As a result, the annual cycle of the subtropical Smax is synchronized to the annual cycle of the tropical Smin, with a phase lag of six months that is regulated by the time needed by the Ekman transport to carry the near-equatorial low salinity waters to the peripheral of the Smax centers.

Two key characteristics are essential in understanding this advective oceanic pathway facilitated by Ekman transport. The first is the source of the freshwater necessary for the generation of near-equatorial low-salinity waters in each ocean basin. The study found that these low-salinity waters are formed beneath the rainfall bands associated with the dITCZ straddling the equator. The rainbands of the northern ITCZ exhibit a persistent and dominant presence, leading to a seasonal Smin of $\sim$ 0.5 pss in September-October in the equatorial Pacific and Atlantic oceans. On the other hand, the rainbands associated with the southern ITCZ are more transient and short-lived, being most evident in March-April. The resultant seasonal amplitude of SSS is relatively weaker, averaging below 0.3 pss. The dITCZ is weak in the Indian Ocean, noticeable only during monsoon transitions in April-May and October-November.

The second feature is the advection time taken by Ekman transport traveling at an average speed of approximately 7 cm s^{-1}. This speed allows the near-equatorial salinity anomalies to be carried to the subtropical *Smax* fringes in six months, aligning closely with the observed semi-annual phase shift in the annual cycles between *Smin* and *Smax*. This reinforces the crucial role of Ekman transport as a mechanism in establishing and maintaining this synchronization.

Additionally, the study revealed two important features. One is that the five subtropical Smax centers all fall within the domain of the poleward meridional Ekman transport that is defined by the zero crossing of the meridional Ekman transport; the latter is referred to as the Ekman impact zone in this study. The second is that the distance between the Smin zone and the Smax center is about 11–12° of latitude in all basins, which equals roughly to the distance that tropical salinity anomalies can be advected by the Ekman transport in six months. It is well known that the *Smax* centers are located within the net evaporation regimes, because these high salinity centers owe their existence to the evaporative forcing of the subtropical regions. The existence of the Ekman impact zone in surface salinity stresses the important role of tropical freshwater forcing in counterbalancing the effects of net evaporation forcing in the subtropical region. Thus, it is not a surprise to find that the Ekman convergence line and the zero E-P line set the poleward boundary for the location of a subtropical Smax center.

Furthermore, the study showed that the poleward Ekman transport plays an important role of spreading the ENSO influence beyond the equatorial region. Over the past decade of satellite salinity missions, the tropical Pacific has experienced strong 2015–2016 El Niño event amidst milder warm episodes, followed by a triple-dip La Niña events in 2020–2023. These exceptional conditions caused a shift in the position and intensity of the dITCZ, and the resultant rainfall anomalies produced substantial surface freshening in the equatorial region. This, in turn, led to considerable poleward propagation of surface low-salinity anomalies, impacting subtropical oceanic conditions. It is particularly intriguing that the ENSO-induced surface freshening remained well within the impact regime of Ekman transport, reaffirming the intrinsic connection between the tropical *Smin* and subtropical *Smax* regions.

In conclusion, this study has a potential to broaden the understanding of the complex interaction between oceanic processes, the water cycle, and the distribution of SSS anomalies. The findings bring to

light the interconnected nature of the tropical *Smin* and subtropical *Smax*, challenging the prevailing notion of treating them as separate entities. Moreover, the findings question conventional thinking regarding the use of salinity as a rain gauge, as it suggests that relying solely on the contrast between these two salinity extrema as a standard measure for assessing the amplification of the water cycle may not be appropriate. Consequently, these insights highlight the need for a reconsideration of methodologies when extracting information about changes in the ocean water cycle from SSS observations. These insights contribute to the ongoing refinement of our perception regarding the intricate interaction between salinity, ocean dynamics, and the water cycle.

Declaration of competing interest

The authors declare that they have no known competing financial interests or personal relationships that could have appeared to influence the work reported in this paper.

Data availability

Data will be made available on request.

Acknowledgements

The author acknowledges the funding support of NASA Ocean Salinity Science Team (OSST) activities through Grants 80NSSC18K1335 and 80NSSC22K0996; NASA Making Earth System Data Records for Use in Research Environments (MEaSUREs) Program, Grant 80NSSC18M0079; and NOAA Global Ocean Monitoring and Observing (GOMO) program, Grant NA19OAR4320074. Data producers for the following datasets are sincerely thanked: OISSS (https://podaac.jpl.nasa.gov/dataset/OISSS_L4_multimission_7day_v1), Argo gridded salinity and temperature analysis (http://sio-argo.ucsd.edu/RG_Climatology.html), precipitation from GPCP Level 3 Monthly 0.5-Degree version 3.2 (https://measures.gesdisc.eosdis.nasa.gov/data/GPCP/GPCPMON.3.2/), and surface evaporation and wind from the OAFlux high-resolution analysis (http://oaflux.whoi.edu).

References

Alory, G., Maes, C., Delcroix, T., Reul, N., Illig, S., 2012. Seasonal dynamics of sea surface salinity off Panama: The far Eastern Pacific Fresh Pool. J. Geophys. Res. Oceans 117, C04028. https://doi.org/10.1029/2011JC007802.

Aubone, N., Palma, E.D., Piola, A.R., 2021. The surface salinity maximum of the South Atlantic. Progr. Oceanogr. 191, 102499 https://doi.org/10.1016/j.pocean.2020.102499.

Bingham, F.M., Foltz, G.R., McPhaden, M.J., 2012. Characteristics of the seasonal cycle of surface layer salinity in the global ocean. Ocean Science 8 (5), 915.

Bingham, F.M., Busecke, J., Gordon, A.L., Giulivi, C.F., Li, Z., 2014. The North Atlantic subtropical surface salinity maximum as observed by Aquarius. J. Geophys. Res. Oceans 119, 7741–7755. https://doi.org/10.1002/2014JC0098.

Boyer, T. P., Levitus, S., Antonov, J. I., Locarnini, R. A., Garcia, H. E., 2005. Linear trends in salinity for the World Ocean, 1955–1998. Geophys. Res. Lett., 32, L01604, https://doi.org/ 10.1029/2004GL021791.

Boyer, T.P., Levitus, S., 2002. Harmonic analysis of climatological sea surface salinity. J. Geophys. Res. Oceans 107 (C12), 7. https://doi.org/10.1029/2001JC000829.

Bryan, F., Bachman, S., 2015. Isohaline salinity budget of the north Atlantic salinity maximum. J. Phys. Oceanogr. 45, 724–736. https://doi.org/10.1175/JPO-D-14-0172.1.

Busecke, J., Abernathey, R.P., Gordon, A.L., 2017. Lateral eddy mixing in the subtropical salinity maxima of the global ocean. J. Phys. Oceanogr. 47 (4), 737–754. https://doi.org/10.1175/JPO-D-16-0215.1.

Camara, I., Kolodziejczyk, N., Mignot, J., Lazar, A., Gaye, A.T., 2015. On the seasonal variations of salinity of the tropical Atlantic mixed layer. J. Geophys. Res. Oceans 120, 4441–4462. https://doi.org/10.1002/2015JC010865.

Cheng, L., Trenberth, K.E., Gruber, N., Abraham, J.P., Fasullo, et al., 2020. Improved estimates of changes in upper ocean salinity and the hydrological cycle. J. Clim. 33, 10357–10381. https://doi.org/10.1175/JCLI-D-20-0366.1.

de Boyer Montegut, C., Madec, G., Fischer, A.S., Lazar, A., Iudicone, D., 2004. Mixed layer depth over the global ocean: An examination of profile data and a profile-based climatology. J. Geophys. Res. 109, C12003. https://doi.org/10.1029/2004JC002378.

Delcroix, T., Henin, C., 1991. Seasonal and interannual variations of sea-surface salinity in the tropical Pacific Ocean. J. Geophys. Res. 96 (C12), 22135–22150.

Delcroix, T., Henin, C., Porte, V., Arkin, P., 1996. Precipitation and sea surface salinity in the tropical Pacific. Deep Sea Res. 43, 1123–1141.

Dickson, R.R., Meincke, J., Malmberg, S.A., Lee, A.J., 1988. The "great salinity anomaly'' in the northern North Atlantic 1968–1982. Prog. Oceanogr. 20 (2), 103–151.

Durack, P.J., Wijffels, S.E., 2010. Fifty-year trends in global ocean salinities and their relationship to broad-scale warming. J. Climate 23, 4342–4362. https://doi.org/10.1175/2010JCLI3377.1.

Durack, P.J., Wijffels, S.E., Matear, R.J., 2012. Ocean salinities reveal strong global water cycle intensification during 1950 to 2000. Science 336, 455–458. https://doi.org/10.1126/science.1212222.

Farneti, R., Dwivedi, S., Kucharski, F., Molteni, F., Griffies, S.M., 2014. On Pacific subtropical cell variability over the second half of the twentieth century. J. Climate 27 (18), 7102–7112. https://doi.org/10.1175/JCLI-D-13-00707.1.

Fine, R. A., Maillet, K. A., Sullivan, K. F., Willey, D., 2001, Circulation and ventilation flux of the Pacific Ocean, J. Geophys. Res., 106(C10), 22 159–22 178.

Gordon, A.L., Giulivi, C.F., 2014. Ocean eddy freshwater flux convergence into the North Atlantic subtropics. J. Geophys. Res. Oceans 119, 3327–3335. https://doi.org/10.1002/2013JC009596.

Gordon, A.L., Giulivi, C.F., Busecke, J., Bingham, F.M., 2015. Differences among subtropical surface salinity patterns. Oceanography 28 (1), 32–39.

Grodsky, S.A., Carton, J.A., 2003. Intertropical convergence zone in the South Atlantic and the equatorial cold tongue. J. Climate 16, 723–733.

Gu, D., Philander, S.G.H., 1997. Interdecadal climate fluctuations that depend on exchanges between the tropics and extratropics. Science 275 (5301), 805–807. https://doi.org/10.1126/science.275.5301.805.

Guimbard, S., Reul, N., Chapron, B., Umbert, M., Maes, C., 2017. Seasonal and interannual variability of the Eastern Tropical Pacific Fresh Pool. J. Geophys. Res. Oceans 122, 1749–1771. https://doi.org/10.1002/2016JC012130.

Halpern, D., Hung, C.-W., 2001. Satellite observations of the southeast Pacific intertropical convergence zone during 1993 – 1998. J. Geophys. Res.,106, 28,107–28,112.

Hasson, A., Delcroix, T., Boutin, J., 2013. Formation and variability of the South Pacific Sea Surface Salinity maximum in recent decades. J. Geophys. Res. Oceans 118, 5109–5116. https://doi.org/10.1002/jgrc.20367.

Hasson, A., Puy, M., Boutin, J., Guilyardi, E., Morrow, R., 2018. Northward pathway across the tropical North Pacific Ocean revealed by surface salinity: How do El Ni~no anomalies reach Hawaii? J. Geophys. Res. Oceans 123, 2697–2715. https://doi.org/10.1002/2017JC013423.

Held, I.M., Soden, B.J., 2006. Robust responses of the hydrological cycle to global warming. J. Climate 19, 5686–5699. https://doi.org/10.1175/JCLI3990.1.

Hubert, L.F., Krueger, A.F., Winston, J.S., 1969. The double intertropical convergence zone–- fact or friction? J. Atmos. Sci. 26, 771–773.

Huffman, G. J., Adler, R. F., Behrangi, A., Bolvin, D. T., Nelkin, E., Song, Y., 2020. Algorithm Theoretical Basis Document (ATBD) for Global Precipitation Climatology Project Version 3.1 Precipitation Data. Available from https://docserver.gesdisc.eosdis.nasa.gov/public/project/MEaSUREs/GPCP/GPCP_ATBD_V3.1.pdf.

Johnson, B.K., Bryan, F.O., Grodsky, S.A., Carton, J.A., 2016. Climatological Annual Cycle of the Salinity Budgets of the Subtropical Maxima. J. Phys. Oceanogr. 46, 2981–2994. https://doi.org/10.1175/JPO-D-15-0202.1.

Jones, C.S., Cessi, P., 2017. Size matters: Another reason why the Atlantic is saltier than the Pacific. J. Phys. Oceanogr. 47 (11), 2843–2859. https://doi.org/10.1175/jpo-d-17-0075.1.

Kao, H.-Y., Lagerloef, G.S.E., 2015. Salinity fronts in the tropical Pacific Ocean. J. Geophys. Res. Oceans 120, 1096–1106. https://doi.org/10.1002/2014JC010114.

Kleeman, R., McCreary, J.P., Klinger, B.A., 1999. A mechanism for generating ENSO decadal variability. Geophys. Res. Lett. 26 (12), 1743. https://doi.org/10.1029/1999GL900352.

Köhler, J., Martins, M.S., Serra, N., Stammer, D., 2015. Quality assessment of spaceborne sea surface salinity observations over the northern North Atlantic. J. Geophys. Res. Oceans 120, 94–112. https://doi.org/10.1002/2014JC010067.

Kolodziejczyk, N., Gaillard, F., 2013. Variability of the heat and salt budget in the subtropical south-eastern pacific mixed layer between 2004 and 2010: Spice Injection Mechanism. J. Phys. Oceanogr 43, 1880–1898. https://doi.org/10.1175/JPO-D-13-04.1.

Kraus, E. B., Turner, J. S.,1967. A one-dimensional model of the seasonal thermocline II. The general theory and its consequences. Tellus, 19 (1). 98-106 doi:10.3402/tellusa.v19i1.9753.

Lietzke, C.E., Deser, C., Vonder Haar, T.H., 2001. Evolutionary structure of the eastern Pacific double ITCZ based on satellite moisture profile retrievals. J. Clim. 14 (5), 743–751. https://doi.org/10.1175/1520-0442(2001)014<0743:ESOTEP >2.0.CO;2.

Liu, W.T., Xie, X., 2002. Double intertropical convergence zones—a new look using scatterometer. Geophys. Res. Lett. 29 (22), 2072. https://doi.org/10.1029/2002GL015431.

Maes, C., Reul, N., Behringer, D., O'kane, T., 2014. The salinity signature of the equatorial Pacific cold tongue as revealed by the satellite SMOS mission. Geoscience Letters 1 (1). https://doi.org/10.1186/s40562-014-0017-5.

Martins, M.S., Stammer, D., 2015. Pacific Ocean surface freshwater variability underneath the double ITCZ as seen by satellite sea surface salinity retrievals. J. Geophys. Res. Oceans 120, 5870–5885. https://doi.org/10.1002/2015JC010895.

Masunaga, H., L'Ecuyer, T.S., 2010. The southeast Pacific warm band and double ITCZ. J. Clim. 23 (5), 1189–1208. https://doi.org/10.1175/2009JCLI3124.1.

Maximenko, N.A., Niiler, P., Rio, M.-H., Melnichenko, O., Centurioni, L., Chambers, D., Zlotnicki, V., Galperin, B., 2009. Mean dynamic topography of the ocean derived

from satellite and drifting buoy data using three different techniques. J. Atmos. Oceanic Technol. 26 (9), 1910–1919.
McCreary, J.P., Lu, P., 1994. Interaction between the subtropical and equatorial ocean circulations: The subtropical cell. J. Phys. Oceanogr. 24 (2), 466–497. https://doi.org/10.1175/1520-0485(1994)024<0466:IBTSAE>2.0.CO;2.
McPhaden, M.J., Zhang, D., 2002. Slowdown of the meridional overturning circulation in the upper Pacific Ocean. Nature 415, 603–608. https://doi.org/10.1038/415603a.
Melnichenko, O.V., Hacker, P., Bingham, F., Lee, T., 2019. Patterns of SSS variability in the eastern tropical Pacific: intra-seasonal to inter-annual time-scales from seven years of NASA satellite data. Oceanography 32 (2), 20–29. https://doi.org/10.5670/oceanog.2019.208.
Melnichenko, O., 2021. Multi-mission L4 Optimally Interpoated Sea Surface Salinity. Ver. 1.0. PO.DAAC, CA, USA. Dataset accessed [2023-05-26] at https://doi.org/10.5067/SMP10-4U7CS.
Melzer, B.A., Subrahmanyam, B., 2017. Decadal changes in salinity in the oceanic subtropical gyres. J. Geophys. Res. Oceans 122, 336–354. https://doi.org/10.1002/2016JC012243.
Mignot, J., Frankignoul, C., 2003. On the interannual variability of surface salinity in the Atlantic. Clim. Dyn. 20, 555–565.
Niiler, P.P., Kraus, E.B., 1977. One-dimensional models. In: Kraus, E.B. (Ed.), Modeling and Prediction of the Upper Layers of the Ocean. Pergamon, N. Y., pp. 143–172
Nilsson, J., Langen, P.L., Ferreira, D., Marshall, J., 2013. Ocean basin geometry and the salinification of the Atlantic Ocean. J. Climate 26, 6163–6184. https://doi.org/10.1175/JCLI-D-12-00358.1.
O'Connor, B.M., Fine, R.A., Olson, D.B., 2005. A global comparison of subtropical underwater formation rate. Deep-Sea Res. 52, 1569–1590.
Pedlosky, J., 1996. Ocean circulation theory. Springer-Verlag, ISBN. 3-540-60489-8, 453pp.
Phillips, H.E., Tandon, A., Furue, R., Hood, R., Ummenhofer, C.C., et al., 2021. Progress in understanding of Indian Ocean circulation, variability, air–sea exchange, and impacts on biogeochemistry. Ocean Sci. 17, 1677–1751. https://doi.org/10.5194/os-17-1677-2021.
Ponte, R.M., Vinogradova, N.T., 2016. An assessment of basic processes controlling mean surface salinity over the global ocean. Geophys. Res. Lett. 43, 7052–7058. https://doi.org/10.1002/2016GL069857.
Qu, T., Gao, S., 2017. Resurfacing of South Pacific tropical water in the equatorial Pacific and its variability associated with ENSO. J. Phys. Oceanogr. 47, 1095–1106.
Qu, T., Gao, S., Fukumori, I., 2011. What governs the North Atlantic salinity maximum in a global GCM? Geophys. Res. Lett. 38, L07602. https://doi.org/10.1029/2011GL046757.
Qu, T., Gao, S., Fine, R.A., 2013. Subduction of south Pacific tropical water and its equatorward pathways as shown by a simulated passive tracer. J. Phys. Oceanogr. 43, 1551–1565. https://doi.org/10.1175/JPO-D-12-0180.1.
Qu, T., Lian, Z., Nie, X., Wei, Z., 2019. Eddy-induced meridional salt flux and its impacts on the sea surface salinity maxima in the southern subtropical oceans. Geophys. Res. Lett. 46, 11292–11300. https://doi.org/10.1029/2019GL084807.
Rao, R.R., Sivakumar, R., 2003. Seasonal variability of sea surface salinity and salt budget of the mixed layer of the north Indian Ocean. J. Geophys. Res. 108 (C1), 3009. https://doi.org/10.1029/2001JC000907.
Reagan, J., Boyer, T., Antonov, J., Zweng, M., 2014. Comparison analysis between Aquarius sea surface salinity and World Ocean Database in situ analyzed sea surface salinity. J. Geophys. Res. Oceans 119, 8122–8140. https://doi.org/10.1002/2014JC009961.
Ren, L., Riser, S.C., 2009. Seasonal salt budget in the northeast Pacific Ocean. J. Geophys. Res. 114, C12004. https://doi.org/10.1029/2009JC005307.
Reul, N., Grodsky, S.A., Arias, M., Boutin, J., Catany, R., Chapron, B., et al., 2020. Sea surface salinity estimates from spaceborne L-band radiometers: An overview of the first decade of observation (2010–2019). Remote Sens. Environ. 242, 111769 https://doi.org/10.1016/j.rse.2020.111769.
Roach, C.J., Balwada, D., Speer, K., 2018. Global observations of horizontal mixing from Argo float and surface drifter trajectories. J. Geophys. Res. Oceans 123, 4560–4575. https://doi.org/10.1029/2018JC013750.
Rochford, D.J., 1964. Salinity maxima in the upper 1000 metres of the North Indian Ocean. Mar. Freshwater Res. 15, 1–24. https://doi.org/10.1071/MF9640001.
Roemmich, D., Alford, M.H., Claustre, H., Johnson, K., King, B., Moum, J., et al., 2019. On the future of Argo: A global, full-depth, multi-disciplinary array. Front. Mar. Sci 6 (439). https://doi.org/10.3389/fmars.2019.00439.
Roemmich, D., Gilson, J., 2009. The 2004–2008 mean and annual cycle of temperature, salinity, and steric height in the global ocean from the Argo Program. Prog. Oceanogr. 82, 81–100.
Schanze, J.J., Schmitt, R.W., Yu, L., 2010. The global oceanic freshwater cycle: A state-of-the-art quantification. J. Mar. Res. 68, 569–595. https://doi.org/10.1357/002224010794657164.
Schmitt, R.W., 2008. Salinity and the global water cycle. Oceanography 21, 12–19. https://doi.org/10.5670/oceanog. 2008.63.
Schott, F. A., J. P. McCreary Jr., and G. C. Johnson, 2004: Shallow overturning circulations of the tropical-subtropical oceans. Earth's Climate: The Ocean-Atmosphere Interaction, Geophys. Monogr., 147, Amer. Geophys. Union, 261–304.
Schott, F., McCreary, J.P., 2001. The monsoon circulation of the Indian Ocean. Prog. Oceanogr. 51 (1), 1–123. https://doi.org/10.1016/S0079-6611(01)00083-0.
Seager, R., Murtugudde, R., Naik, N., Clement, A., Gordon, N., Miller, J., 2003. Air–sea interaction and the seasonal cycle of the subtropical anticyclones. J. Climate 16 (12), 1948–1966. https://doi.org/10.1175/1520-0442(2003)016<1948:AIATSC>2.0.CO;2.
Shcherbina, A.Y., D'Asaro, E.A., Riser, S.C., Kessler, W.S., 2015. Variability and interleaving of upper-ocean water masses surrounding the North Atlantic salinity maximum. Oceanography 28 (1), 106–113. https://doi.org/10.5670/oceanog.2015.12.
Solomon, A., 2010. Interannual ENSO variability forced through coupled atmosphere–ocean feedback loops. Geophys. Res. Lett. 37, L02706. https://doi.org/10.1029/2009GL041622.
Tchilibou, M., Delcroix, T., Alory, G., Arnault, S., Reverdin, G., 2015. Variations of the tropical Atlantic and Pacific SSS minimum zones and their relations to the ITCZ and SPCZ rain bands (1979–2009). J. Geophys. Res. Oceans 120, 5090–5100. https://doi.org/10.1002/2015JC010836.
Terray, L., Corre, L., Cravatte, S., Delcroix, T., Reverdin, G., Ribes, A., 2012. Near-surface salinity as nature's rain gauge to detect human influence on the tropical water cycle. J. Climate 25, 958–977. https://doi.org/10.1175/JCLI-D-10-05025.1.
Vinogradova, N., Lee, T., Boutin, J., Drushka, K., Fournier, S., Sabia, R., et al., 2019. Satellite salinity observing system: Recent discoveries and the way forward. Front. Mar. Sci. 6, 243. https://doi.org/10.3389/fmars.2019.00243.
Vinogradova, N.T., Ponte, R.M., 2013. Clarifying the link between surface salinity and freshwater fluxes on monthly to interannual time scales. J. Geophys. Res. Oceans 118, 3190–3201. https://doi.org/10.1002/jgrc.20200.
Vinogradova, N.T., Ponte, R.M., 2017. In search of fingerprints of the recent intensification of the ocean water cycle. J. Climate 30, 5513–5528. https://doi.org/10.1175/JCLI-D-16-0626.1.
Walin, G., 1982. On the relation between sea-surface heat flow and thermal circulation in the ocean. Tellus 34 (2), 187–195.
Waliser, D.E., Gautier, C., 1993. A satellite-derived climatology of the ITCZ. J. Climate 6, 2162–2174.
Wang, Y., Li, Y., Wei, C., 2020. Subtropical sea surface salinity maxima in the South Indian Ocean. J. Ocean. Limnol. 38, 16–29. https://doi.org/10.1007/s00343-019-8251-5.
Yu, L., 2011. A global relationship between the ocean water cycle and near-surface salinity. J. Geophys. Res. Oceans 116. C10025.https://doi.org/10.1029/2010jc006937.
Yu, L., 2014. Coherent evidence from Aquarius and Argo for the existence of a shallow low-salinity convergence zone beneath the Pacific ITCZ. J. Geophys. Res. Oceans 119, 7625–7644. https://doi.org/10.1002/2014JC010030.
Yu, L., 2015. Sea-surface salinity fronts and associated salinity-minimum zones in the tropical ocean. J. Geophys. Res. Oceans 120 (6), 4205–4225. https://doi.org/10.1002/2015JC010790Yu, L. (2015).
Yu, L., Bingham, F. M., Lee, T., Dinnat, E. P., Fournier, S., Melnichenko, O., Tang, W., Yueh, S. H., 2021. Revisiting the global patterns of seasonal cycle in sea surface salinity. J. Geophys. Res. Oceans, 126, e2020JC016789. https://doi.org/10.1029/2020JC016789.
Yu, L., Jin, X., Liu, H., 2018. Poleward shift in ventilation of the North Atlantic subtropical underwater. Geophys. Res. Lett. 45 https://doi.org/10.1002/2017GL075772.
Yu, L., Josey, S.A., Bingham, F.M., Lee, T., 2020. Intensification of the global water cycle and evidence from ocean salinity: A synthesis review. Ann. N. Y. Acad. Sci. 1472, 76–94. https://doi.org/10.1111/nyas.14354.
Zhang, C., 2001. Double ITCZs. J. Geophys. Res. 106 (D11), 11785–11792. https://doi.org/10.1029/2001JD900046.
Zhong, W., Cai, W., Zheng, X.-T., Yang, S., 2019. Unusual anomaly pattern of the 2015/2016 extreme El Niño induced by the 2014 warm condition. Geophys. Res. Lett. 46, 14772–14781. https://doi.org/10.1029/2019GL085681.
Zika, J.D., Skliris, N., Nurser, A.J.G., Josey, S.A., Mudryk, L., Laliberté, F., Marsh, R., 2015. Maintenance and Broadening of the Ocean's Salinity Distribution by the Water Cycle. J. Climate 28, 9550–9560. https://doi.org/10.1175/JCLI-D-15-0273.1.